

The Pennsylvania State University
The Graduate School
College of Earth and Mineral Sciences

**THE IMPACT OF IRON CONCENTRATION ON THE PROPERTIES OF AN
ADDITIVELY MANUFACTURED SOLID SOLUTION STRENGTHENED NICKEL
BASE ALLOY**

A Thesis in
Materials Science and Engineering
by
Zakariya R. Khayat

© 2017 Zakariya R. Khayat

Submitted in Partial Fulfillment
of the Requirements
for the Degree of

Master of Science

December 2017

The thesis of Zakariya R. Khayat was reviewed and approved* by the following:

Todd A. Palmer
Professor of Materials Science and Engineering
Professor of Engineering Science and Mechanics
Thesis Adviser

Allison Beese
Assistant Professor of Materials Science and Engineering

Reginald F. Hamilton
Associate Professor of Engineering Science and Mechanics

Jingjing Li
Associate Professor of Industrial and Manufacturing Engineering

Jayme Keist
Research Associate of the Applied Research Laboratory at Penn State University
Special Signatory

Suzanne Mohny
Professor of Materials Science and Engineering and Electrical Engineering
Chair, Intercollege Graduate Degree Program in Materials Science and Engineering

*Signatures are on file in the Graduate School

ABSTRACT

Additive manufacturing (AM) technology is capable of producing free-form geometries for large scale applications. Fabricating entire structures in a continuous layer-by-layer fashion can mitigate possible material property mismatch problems that have been noted in various welding operation studies. Inconel® 625 would be primarily used as the overlay material in a weld clad because of the high corrosion and wear resistance it exhibits. However, instead of only adding a few layers of material to a dissimilar base material, there is interest in using AM to process entire components made from Ni base alloys that will exhibit the material properties in bulk form.

Alloying element compositions in Inconel® 625 can vary over rather wide ranges, with Fe, in particular, ranging from 0 to 5 wt%. The impact of changes in the Fe content on the properties of AM materials is investigated using a series of laser-based directed energy deposited (DED) builds with Fe contents of 1 wt% and 4 wt% in both the as deposited and post processed hot isostatically pressed (HIP) conditions. While similar solidification structures and microhardness values of the fabricated builds are observed with both powder feedstocks, the low Fe content feedstock samples displayed higher yield ($520 \text{ MPa} \pm 12 \text{ MPa}$) and tensile strengths ($860 \text{ MPa} \pm 27 \text{ MPa}$) and lower elongation values ($36 \% \pm 5 \%$) in the as-deposited condition compared to yield ($450 \text{ MPa} \pm 27 \text{ MPa}$) and tensile strengths ($753 \text{ MPa} \pm 25 \text{ MPa}$) and elongation values ($44 \% \pm 9 \%$) with the high Fe content feedstock samples. The differences in mechanical properties were highly dependent on the condition and were connected to differences in the strengthening mechanisms associated with the two different Inconel® 625 powder compositions.

Low Fe content samples had an average grain size 10x smaller than that of high Fe content samples in the as deposited condition, which led to differences in mechanical properties. After HIP, Low Fe content samples displayed smaller grains, but compared to the as deposited condition, there was not substantial grain growth or recrystallization. The yield strength of both low and high Fe content builds decreased by 14%, while elongation increased by 15%. While on the other hand, post processed tensile strengths changed by only 3%. This small change in tensile strength can be traced to higher levels of strain hardening for high Fe content feedstocks. These differences in mechanical behavior can be attributed in part, to changes in precipitate formation after HIP. It is speculated that in low Fe content samples large Nb and Mo rich precipitates form that pin grain

boundary motion while in the high Fe content samples, tiny Ti rich precipitates form that pin dislocation motion.

Precipitate formation is denoted as secondary phase formation. In order to study the impact alloying elements had on the resulting secondary phase constituents, thermodynamic phase stability calculations were conducted. Calculations showed different phase formation tendencies for each powder feedstock material. In addition, phase stability calculations helped set guidelines in order to distinguish between secondary phase constituents based upon the Nb content. Coupled with a low C/Nb ratio and verified using an electron probe microanalysis (EPMA), secondary phase constituents were characterized as Laves phase.

TABLE OF CONTENTS

LIST OF FIGURES	vii
LIST OF TABLES	x
ACKNOWLEDGEMENTS	xi
Chapter 1 INTRODUCTION.....	1
1.1 Background	1
1.2 Motivation	4
1.3 Objectives.....	4
1.4 Thesis Structure.....	5
Chapter 2 LITERATURE REVIEW	6
2.1 Introduction	6
2.2 The Impact of Alloying Elements on Secondary Phase Formation	6
2.3 The Impact of Secondary Phase on Material Properties	8
2.4 Directed Energy Deposition of Inconel® 625.....	9
Chapter 3 EXPERIMENTAL PROCEDURE	11
3.1 Powder Feedstock Characterization	11
3.2 Directed Energy Deposition Setup.....	11
3.3 Deposition Processing Parameters	13
3.4 Microstructural Characterization.....	14
3.4.1 Metallurgical Preparation	14
3.4.2 Secondary Dendrite Arm Spacing	15
3.4.3 Secondary Phase Volume Fraction Analysis.....	15
3.5 Elemental Composition Measurements.....	16
3.6 Grain Size Measurements.....	17
3.7 Mechanical Property Characterization	17
3.7.1 Strain Hardening Coefficient Measurements	19
Chapter 4 ANALYSIS OF STRUCTURES IN THE AS DEPOSITED CONDITION	21
4.1 Powder Feedstock Characterization	21
4.2 Analysis of Fabricated Structures	22
4.3 Summary and Conclusions.....	30
Chapter 5 ANALYSIS OF STRUCTURES IN THE HOT ISOSTATIC PRESSED CONDITION	32
5.1 Characterization of Post Processed Structures	32
5.2 Summary and Conclusions.....	39
Chapter 6 THEORIETICAL ANALYSIS OF PHASE STABILITY	41
6.1 Thermodynamic and Microstructural Characterization of the As Deposited Condition	41
6.1.1 Thermodynamic Stability	41
6.1.2 Characterization of the Secondary Phase	46
6.2 Thermodynamic and Microstructural Characterization of the HIP Condition.....	47

6.2.1 Thermodynamic Stability	47
6.2.2 Microstructural Characterization of Secondary Phase Constituents	48
6.3 Summary and Conclusions.....	50
Chapter 7 CONCLUDING REMARKS	51
7.1 Summary and Conclusions.....	51
7.2 Future Work	52
REFERENCES	54

LIST OF FIGURES

Figure 1.1: (a) A hot rolled annealed Inconel® 625 wrought microstructure. (b) Typical weld-base microstructure displaying the dendritic constituents that are a result of the high growth and cooling rates.	2
Figure 1.2: Micrograph displaying the solidification features that are associated with Inconel® 625 solidification operations.	3
Figure 1.3: (a) General illustration of an AM powder bed system. (b) General illustration of an AM powder feed DED system [19].	4
Figure 2.1: The general solidification process that exhibit both $L \rightarrow (\gamma + \text{NbC})$ and $L \rightarrow (\gamma + \text{Laves})$ eutectic-type reactions. (a) As dendrites grow into the liquid there is an (b) enrichment of Nb and C. (b) Once the saturation limit is reached by the liquid composition, solidification continues however constituents form simultaneously. The exact path depends upon the exact liquid composition. At point (c), the $L \rightarrow (\gamma + \text{NbC})$ reaction is replaced by the $L \rightarrow (\gamma + \text{Laves})$ reaction and the remaining liquid transforms to the γ/Laves eutectic-type constituent as solidification proceeds on to completion (d).[21].....	7
Figure 2.2: A SEM photomicrograph of a Laves phase constituent displaying the lamellar morphology [14].	7
Figure 2.3: TEM image that shows the formation of blocky-like Laves phase and small MC carbides attached to it [13].	8
Figure 2.4: (a) Plot that describes along the build height, the dendrite arm coarsens; (b) plot that describes microhardness values decreased with height.	10
Figure 3.1: (a) Isometric view of the CAD model of the fabricated L shaped test structures via DED along with (b) the build paths for the L shaped structure. Also showing are the locations of where tensile specimens were extracted from in the fabricated structures. Longitudinal specimens are parallel to the substrate and transverse specimens are oriented perpendicularly.	12
Figure 3.2: A representative X-ray CT scan of a fabricated structure (a) before and (b) after conducting a porosity analysis to measure the defects levels in the as deposited condition. Noted in the porosity analysis scan are where defects were detected.	13
Figure 3.3: Image analysis was used to measure the SDAS depicted above. The peaks for the plot profile, where the y-axis is gray value, denote the interdendritic regions. Also denoted in the figure are constituents that form upon solidification	15
Figure 3.4: Image analysis was used to measure the average secondary phase particle size. The threshold technique was used to remove certain features and then determine the size of all the dark colored particles.	16
Figure 3.5: Schematic diagram describing how grain size was determined from the EBSD scans. Also identified in the figure are the major and minor axes.	17
Figure 3.6: Representative tensile specimen that was extracted from the fabricated structures and used for mechanical testing. All measurements are in mm.	18

Figure 3.7: Schematic diagram detailing the location at which tensile specimens were extracted. All measurements are in mm.	19
Figure 4.1: SEM micrograph of the (a) low and (b) high Fe Inconel® 625 nitrogen atomized powder. High Fe content powder particles show presence of satellite formation.	21
Figure 4.2: Particle size distribution curves of low and high Fe powder feedstock material detailing the difference in size and spread between low and high Fe feedstock materials	22
Figure 4.3: Optical microscopy images of low Fe, as deposited. (b) is a magnified micrograph of a representative location to depict the secondary phase formation.....	23
Figure 4.4: Optical microscopy images of high Fe, as deposited. (b) is a magnified micrograph of a representative location to depict the secondary phase formation.....	23
Figure 4.5: SDAS measurements for low and high Fe content samples in the as deposited condition.	24
Figure 4.6: Microhardness measurements of low and high Fe content samples in the as deposited build condition	25
Figure 4.7: Representative engineering stress-strain and true stress-strain curves comparing the impact of Fe content on the strain hardening of Inconel® 625 during tensile testing.....	27
Figure 4.8: Graphs displaying the similar amounts of secondary phase (a) particle size and (b) volume fraction for low and high Fe content samples.....	27
Figure 4.9: EDS maps of (a) low Fe and (b) high Fe in the as deposited detailing the secondary formation enriched in Mo and Nb.....	28
Figure 4.10: EBSD images in the as deposited condition of (a) low Fe and (b) high Fe.	29
Figure 5.1: X-ray CT scans demonstrating the ability of a post processing HIP heat treatment to minimize defect level from the (a) as deposited condition to (b) HIP condition.....	32
Figure 5.2: Optical microscopy image of (a) low Fe, HIP and (b) a magnified image of the secondary phase formation of the representative location within the same sample.	33
Figure 5.3: Optical microscopy image of (a) high Fe, HIP and (b) a magnified image of the secondary phase formation of the representative location within the same sample.	34
Figure 5.4: Secondary phase formation measurements of the (a) average size and (b) volume fraction.	34
Figure 5.5: Microhardness measurements of low and high Fe content samples in the HIP condition.	35
Figure 5.6: EBSD images in the HIP condition of (a) low Fe and (b) high Fe.....	37
Figure 5.7: EDS maps of (a) low Fe and (b) high Fe in the HIP condition detailing the precipitation formation and the dissociation response in low Fe and high Fe.....	38
Figure 5.8: Diagrams describing the possible phenomena occurring in each HIP sample with respect to Fe content. In (a) the low Fe content case, large precipitates are impeding grain boundary motion and in (b) the high Fe content case, small precipitates, distributed readily are impeding dislocation motion.....	39

Figure 6.1: BSE photomicrographs of (a) low and (b) high Fe content microstructures denoting the EPMA line scan across interdendritic regions	42
Figure 6.2: EMPA composition trace conducted across a low Fe content sample dendrite arm..	42
Figure 6.3: EMPA composition trace conducted across a high Fe content sample dendrite arm.	43
Figure 6.4: Thermodynamic calculations that show the influence of various alloying elements (a) Fe; (b) Ti; (c) Si on secondary phase formation.	44
Figure 6.5: Representative wt% compositions of Nb and Mo in specific secondary phases: (a) Laves phase; (b) MC carbide; (c) M ₆ C carbide. Nb wt% can be used to identify which secondary phase is forming after solidification.	45
Figure 6.6: Element composition of Nb wt% in matrix (γ) as a function of temperature. The Nb wt% compositional is higher in the high Fe content Inconel® 625.....	45
Figure 6.7: EPMA chemistry analysis of the resulting secondary phase constituents that formed in the as deposited condition for (a) low Fe and (b) high Fe content samples.	46
Figure 6.8: Scheil calculations of the resulting phase fraction upon solidification for (a) low Fe and (b) high Fe content compositions. The HIP treatment was conducted at 1433 K. MC carbide formation is present in the high Fe content calculation but not for low Fe.	48
Figure 6.9: EPMA chemistry analysis of the resulting secondary phase constituents that formed in the HIP condition for (a) low Fe and (b) high Fe content samples.....	49
Figure 6.10: EPMA chemistry map analysis portraying measureable Ti intensity specifically where black spots are located in the BSE image. The color scale is in wt%.....	50

LIST OF TABLES

Table 1.1: Summary of the general effect of various alloying elements on phase stability for Ni base alloys [3].	1
Table 3.1: Chemical compositions of low and high Fe content Inconel® 625. Standard composition is according to ASTM B705-05.[42]	12
Table 3.2: Powder measurement results from the PSD results and additional powder characterization.	14
Table 4.1: Mechanical property results for low and high Fe, as deposited and HIP, Inconel® 625 tensile specimens. Strain hardening exponent values are calculated and shown as well. Standard values are from Special Metals certification.[2]	26
Table 4.2: Statistical information for grain size and morphology for low and high Fe content builds.....	30
Table 6.1: Chemical compositions of the constituents shown in Figure 6.7.	46
Table 6.2: Chemical compositions of the constituents that formed in the HIP condition.*High Fe content samples do not form Laves phase or carbides.....	49

ACKNOWLEDGEMENTS

In the name of The Most Gracious, The Most Merciful I commenced this journey of discovery. All praise is due to the Most High who has blessed me with innumerable blessings. With His guidance, I have had the opportunity to work with these great people who I want to acknowledge.

First and foremost, I want to acknowledge Dr. Todd Palmer for taking me on as a master's degree student. I thank him for his mentorship that has truly brought my research skills from layman to professional quality. I would also like to thank the research group members of Team TAP: Scott Meredith, Marissa Brennan, Andrew Iams and James Zuback that have helped me along the way. Their academic advice helped me progress as a researcher and their friendship helped me progress as a student and community member. I want to recognize the team from ARL at CIMP-3D. I am grateful for Mr. Ed Good, Mr. Jay Tressler, Mr. Griffin Jones, and Wesley Mitchell for their assistance and training that has aided my research project along the way. I am thankful for Julie Anderson of the Penn State Materials Characterization Laboratory for her expertise in scanning electron microscopy and always having a friendly, warming presence while in the lab.

I was to express my gratitude to my family for their endless support. They have supported me in all my endeavors over the past two years. My mother, spiritually, has always been there for me and helped me stay focused. There is nothing better than seeing your parents proud of you. My father that always pushed me in every aspect of my life is genuinely proud of me and there is nothing more than for me knowing that. My younger brother, Zahare, thank you for keeping me fresh with your Z Cuts hair cutting business. I am grateful to be gifted with having a younger brother. Little Z, you have been someone that has helped me smile, laugh, and stay true to my roots. I would not be where I am today without the unconditional love and prayers from my family.

Lastly, I am indebted to the Department of Energy (EERE FOA-0001006) and the ARL Walker Fellowship for the financial support that enabled me to complete this research.

Chapter 1

INTRODUCTION

1.1 Background

Inconel® 625 is a versatile and widely used Ni-Cr-Fe solid solution strengthened alloy that is known for its combination of high strength, outstanding corrosion resistance, and excellent fabricability [1,2]. Its high resistance to oxidation is produced by the Ni and Cr alloying element additions, while Mo provides corrosion resistance and Nb improves its stiffness [3]. A summary of the impact of alloying elements in Ni-base alloys is shown in Table 1.1.

In the as welded condition, Inconel® 625 maintains its strength and ductility across a wide range of temperatures from cryogenic conditions through temperatures in excess of 980°C [3]. When used in weld overlays on high carbon steels for corrosion and wear resistant applications, Inconel® 625 is able to be diluted by Fe and C yet still maintain its ductility providing good machining characteristics [3]. The weldability of Inconel® 625 has also allowed it to be used as a filler material for dissimilar welds, specifically between carbon steels and austenitic stainless steels, where it provides a smooth transition between the two materials and avoids cracking during the welding process. These properties make Inconel® 625 an attractive candidate for use in a wide range of applications from jet turbine engines, marine components, and chemical processing equipment [4].

Table 1.1: Summary of the general effect of various alloying elements on phase stability for Ni base alloys [3].

Effect	Element
Solid Solution Strengtheners	Co, Cr, Fe, Mo, W, Ta
γ' -Ni ₃ (Al,Ti) Former	Al, Ti
Solid Solution Strengthening of γ'	Cr, Mo, Ti, Si, Nb
γ'' -Ni ₃ Nb Former	Nb
Carbide Formers:	
MC and M(C,N)	W, Ta, Ti, Mo, Nb
M ₇ C ₃	Cr
M ₂₃ C ₆	Cr, Mo, W
M ₆ C	Mo, W

A typical hot rolled, annealed wrought microstructure of Inconel® 625 is shown in Figure 1.1a. During welding, the solidification mode becomes dendritic as shown in Figure 1.1b. The redistribution of alloying elements during solidification can result in the formation of secondary phases. Microstructural features associated with Inconel® 625 solidification operation are denoted in Figure 1.2. These ordered secondary phases, which include various carbides (MC , M_6C , and $M_{23}C_6$) and Laves phase, are shown to have a detrimental impact on mechanical properties [5,6]. Laves phase is a brittle microconstituent composed primarily of Nb and Mo that adversely affects ductility and acts as a crack initiation site [6–12]. Formation of this undesired phase is typically limited by controlling composition. Previous work has been directed at tightly controlling the Si, C, and Nb compositions to limit Laves phase formation. When there is high Si and low C compositions, Laves phase was promoted [5,13]. Increased levels of Nb, for example, were also shown to increase secondary phase constituents as well as the solidification temperature range, which increased crack susceptibility [5].

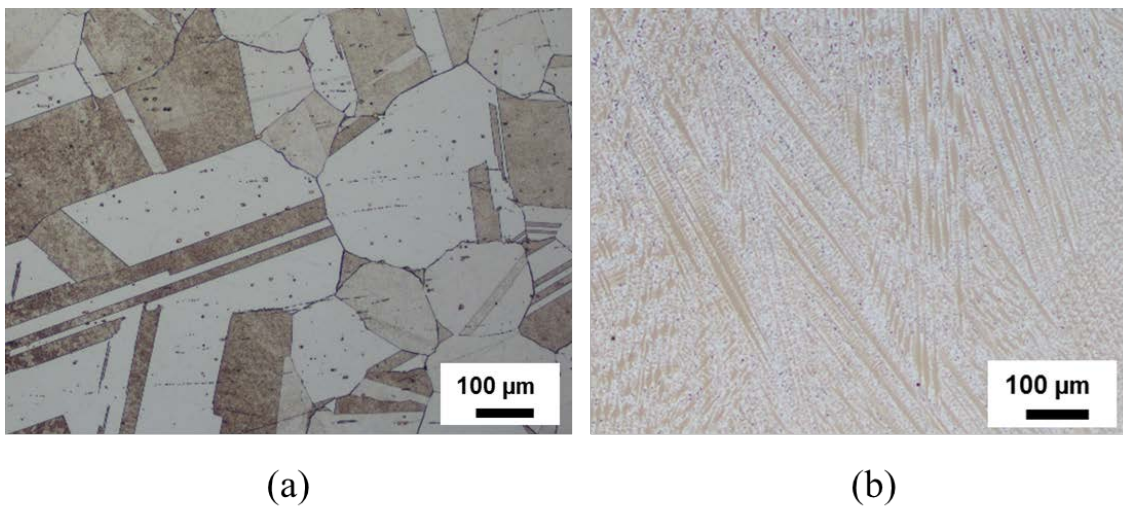


Figure 1.1: (a) A hot rolled annealed Inconel® 625 wrought microstructure. (b) Typical weld-base microstructure displaying the dendritic constituents that are a result of the high growth and cooling rates.

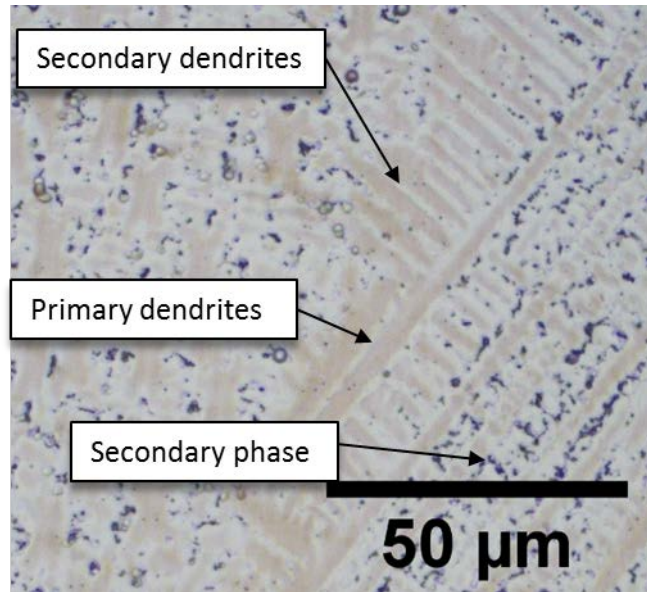


Figure 1.2: Micrograph displaying the solidification features that are associated with Inconel® 625 solidification operations.

The weldability of Inconel® 625 make it an attractive candidate material for additive manufacturing (AM) processes. It has been widely used for welds and clad overlays, which has allowed its solidification kinetics and thermodynamics to be extensively studied and understood [5,13–18]. Expected solidification structures, secondary phase formation, and resulting microstructural properties formed during welding have been identified in much of this work [5,13,14]. With AM processes, it is now possible to fabricate 3-dimensional Inconel® 625 structures with varying levels of geometric complexity. However, the deposited material experiences complex thermal processing cycles, which the solidification path and final microstructure of the material. Since there is limited information presented on large scale AM fabrication for Inconel® 625, there is a limited understanding of the underlying process-structure relationships.

Depending on the geometrical complexities and the required size of the structure there are two categories of AM for metal materials: Powder bed fusion (PBF) and directed energy deposition (DED). Current research interests in the AM field have focused on PBF. These systems, shown in Figure 1.3a, have the ability to produce high resolution features. Due to the small build volume ($< 0.03 \text{ m}^3$), only small scale complex parts can be fabricated [19]. There is a wide range of other potential applications where AM of larger material structures desired. Powder delivered laser based DED systems, shown in Figure 1.3b, allow for larger build volumes than PBF ($> 1.2 \text{ m}^3$) to

be achieved and can improve deposition rates. Powder feedstock material is fed through a co-axial deposition head that is given coordinate points to follow based on the developed program code. This setup includes a laser that rapidly melts and solidifies location specific points on an AM deposit. The laser melts the powder and continues to scan across the deposit in order to complete a layer. This process is repeated and translated vertically until the structure is complete.

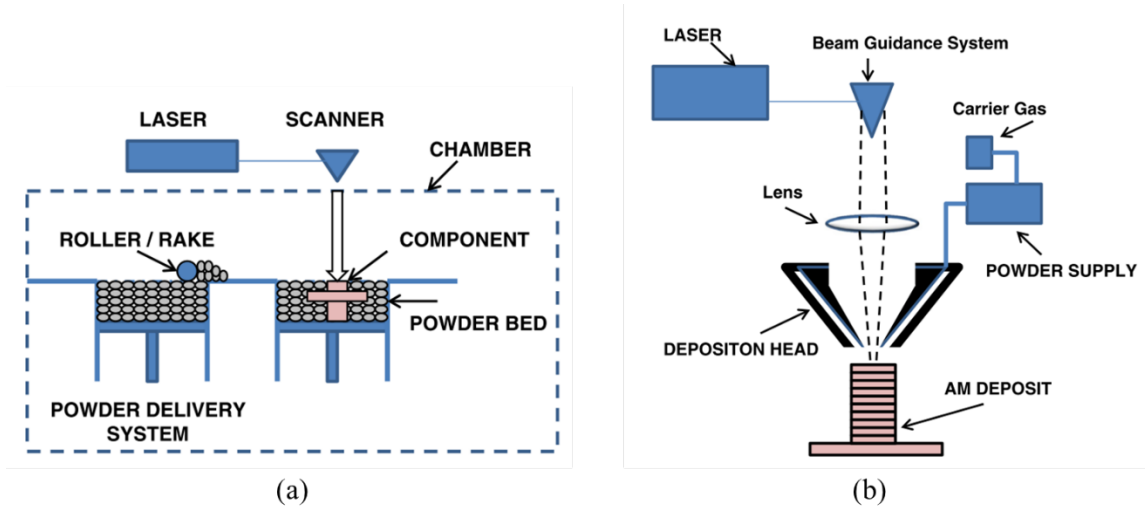


Figure 1.3: (a) General illustration of an AM powder bed system. (b) General illustration of an AM powder feed DED system [19].

1.2 Motivation

The overall goal of this work is to investigate the role Fe content has on DED Inconel® 625 fabricated structures and to shed light on the need to have tighter compositional control to ensure more consistent properties. AM technologies rely on traditional powder processing techniques to produce powder that will be utilized by AM deposition systems. Currently, the industry operates on the assumption that as long as powders meet ASTM specifications governing wrought materials, the powder feedstock material can be used for AM practices and the fabricated structures should behave similarly. The impact of powder processing conditions on AM structures is not well understood.

1.3 Objectives

- To develop an understanding of the role of Fe content has on the properties of DED AM Inconel® 625 structures

- To investigate the impact post processing has the as deposited structures after a hot isostatic press (HIP) cycle was performed.

1.4 Thesis Structure

This research seeks to develop a fundamental understanding of the role Fe composition has on the microstructure, condition, and mechanical properties of an AM Inconel® 625 component. The content of this work is divided into 7 chapters.

In chapter 1, the context of the research project, the motivation and objectives are presented.

In chapter 2, a comprehensive review of the current research on the solidification and microstructural evolution in Inconel® 625 during welding and AM processes is presented.

In chapter 3, the experimental procedure used to fabricate all the structures, the metallurgical preparation, and the characterization and testing methods used are provided.

In chapter 4, the impact of Fe composition on the as deposited structures will be presented. The solidification structures obtained will be studied using various microstructural analyses and the grain sizes associated with the samples will be correlated to the mechanical testing results.

In chapter 5, the role of post processing will be investigated. Precipitate formation after the heat treatment will be studied and the impact it had on the mechanical properties and strengthening mechanisms will be presented.

In chapter 6, thermodynamic calculations were conducted on each powder feedstock material in order to demonstrate that there was an initial difference in solidification between the low and high Fe content materials. Scheil solidification calculations showed differences in the solidification range and based upon the thermodynamic calculations, characterization of the secondary phase, combined with EPMA analyses, is predicted.

In chapter 7, the summary and conclusions of the research are presented. In addition, based on the knowledge gained over the course of the study, future areas of research are suggested.

Chapter 2

LITERATURE REVIEW

2.1 Introduction

Inconel® 625 is a solid-solution strengthened Ni base alloy that obtains its strength from the substitutional alloying of Nb and Fe [8]. Originally designed for applications in steam and gas turbines, the alloy has also seen wide use as a clad or weld overlay in corrosion and wear environments. For example, it is widely used in marine environments, where high corrosion resistance and moderate strength is required [13].

2.2 The Impact of Alloying Elements on Secondary Phase Formation

Alloying element compositional ranges provide versatility to the system and expand the application range. Multiple studies have been conducted to investigate the role Si, Nb, and C alloying elements have on the properties of gas tungsten arc (GTA) weld overlays [5,13,14,20,21]. These studies focused on the impact alloying elements had on the formation of secondary phases. With systematic variations of Nb, Si, and C, DTA and microstructural characterizations showed that Si additions increased the amount of the γ /Laves constituent, C additions promoted the γ /NbC constituent, and the influence of Nb depended on the levels of C. When C content was high, Nb promoted the formation of the γ /NbC constituent, otherwise the γ /Laves constituent formed. Furthermore, dissimilar Inconel® 625 overlays on Cr-Mo steel substrates showed that Laves phase was also promoted specifically due to the dilution of Fe from the substrate [14]. In addition, for Nb-bearing superalloys when Fe content was increased, the Nb distribution coefficient, K_{Nb} , decreased [20]. As a consequence, this behavior led to the promotion of eutectic-type constituents for Fe-rich alloys.

Secondary phase formation is dependent upon the solidification routes, which are shown in Figure 2.1 for Nb-bearing superalloys [21]. The dominating solidification reaction is the enrichment of the remaining interdendritic liquid in Nb, and the consequent formation of Nb-rich Laves phase and/or Nb-rich MC carbides during the final stages of solidification [8]. The Laves phase (A_2B) constituent has a hexagonal crystal structure, in which Cr, Fe, and Ni occupy the A positions, while Si, P, Nb, and Mo occupy the B positions. It has been commonly identified by its lamellar morphology shown in Figure 2.2. In addition to the formation of the Laves phase, NbC,

which has a cubic crystal structure and a spherical morphology could be attached to a Laves phase constituent, as shown in Figure 2.3.

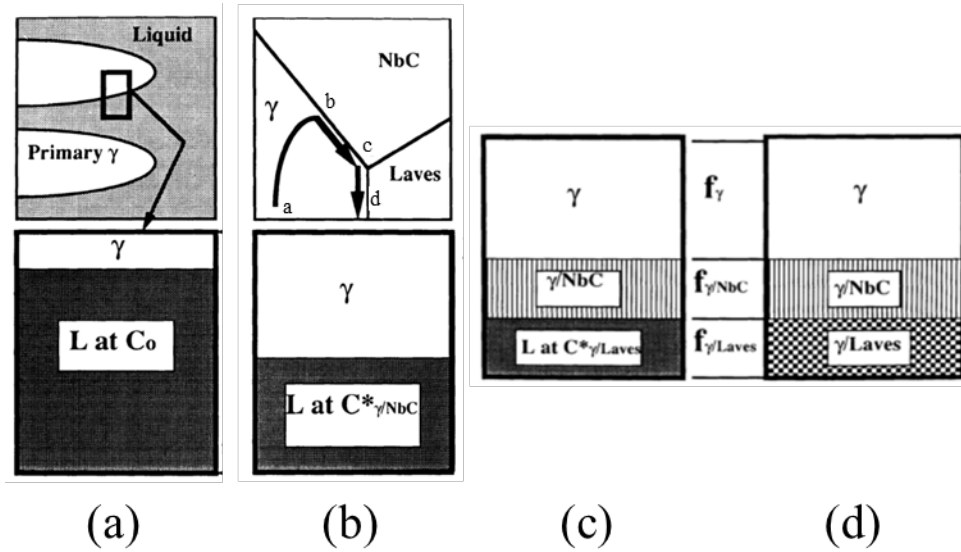


Figure 2.1: The general solidification process that exhibit both $L \rightarrow (\gamma + NbC)$ and $L \rightarrow (\gamma + Laves)$ eutectic-type reactions. (a) As dendrites grow into the liquid there is an (b) enrichment of Nb and C. (b) Once the saturation limit is reached by the liquid composition, solidification continues however constituents form simultaneously. The exact path depends upon the exact liquid composition. At point (c), the $L \rightarrow (\gamma + NbC)$ reaction is replaced by the $L \rightarrow (\gamma + Laves)$ reaction and the remaining liquid transforms to the $\gamma/Laves$ eutectic-type constituent as solidification proceeds on to completion (d).[21]

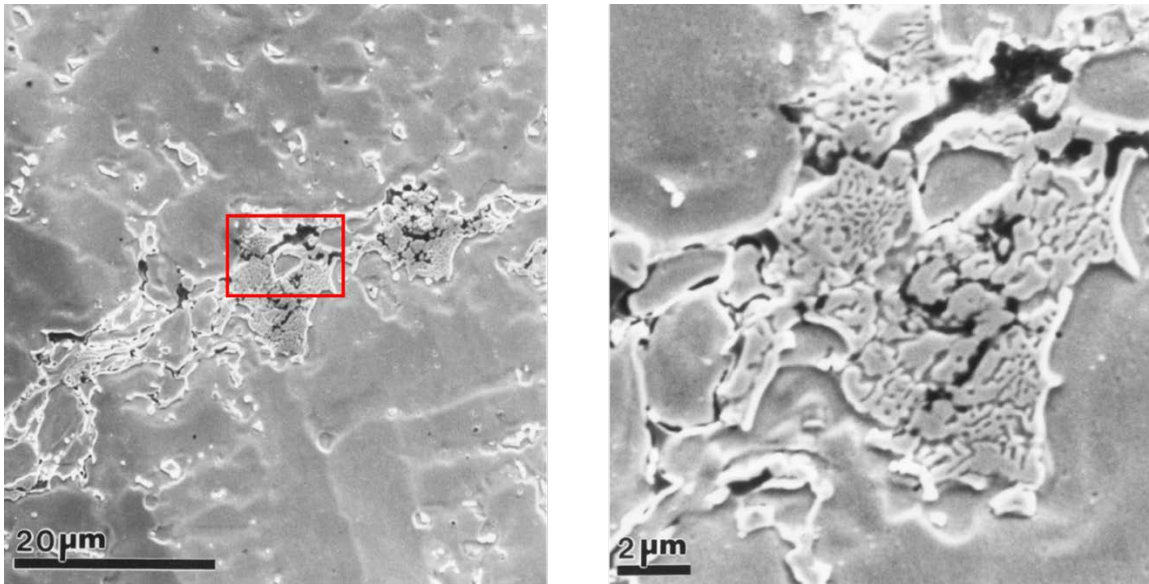


Figure 2.2: A SEM photomicrograph of a Laves phase constituent displaying the lamellar morphology [14].

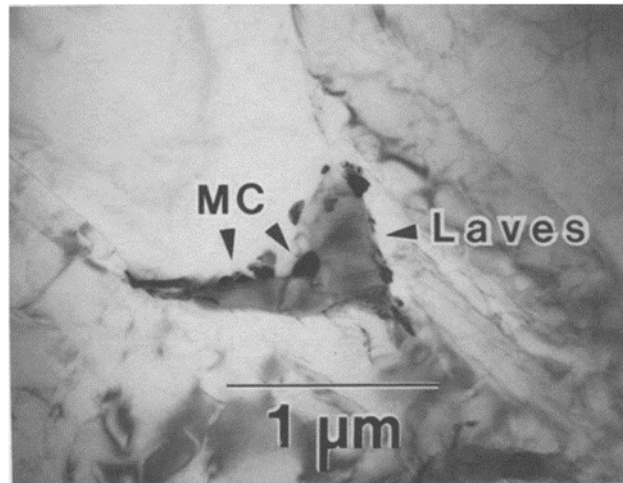


Figure 2.3: TEM image that shows the formation of blocky-like Laves phase and small MC carbides attached to it [13].

Floreen et al. evaluated the roles alloy composition and processing history had on the microstructure and properties of Inconel® 625 [8]. They found that the composition range of Inconel® 625 is overly broad and tighter control of the composition would help ensure more consistent properties between different heats of the alloy. The study recommended that minimizing Nb, Fe, Mo, C, and Si would help improve weldability. However, minimizing C content would promote Laves phase during solidification and minimizing Si content would promote carbide precipitation during heat treatment. Additions of Al and Ti were used for refining purposes and with a sufficient amount of Al and Ti content joined with Nb, precipitation hardening by γ'' could be achieved in Inconel® 625.

2.3 The Impact of Secondary Phase on Material Properties

As the combination of alloying elements is necessary to improve the properties of Inconel® 625, the element additions and subtractions can also be detrimental to the performance of the superalloy. Laves phase is a brittle constituent that adversely affects mechanical performance, specifically, the ductility [6]. When Laves phase is minimized, there are significant improvements to the toughness of the material [8]. In addition, the solidification cracking resistance is decreased with increasing the total minor element content, which is generally attributed to the increased solidification temperature range and tendency to form secondary phases [14]. An increased

solidification range maximizes the amount of segregation of elements during solidification, therefore, diminishing the hot workability.

2.4 Directed Energy Deposition of Inconel® 625

Directed energy deposition (DED) AM of Inconel® 625 has been studied in areas of powder feedstock by varying the sieve range of the feedstock material[22], processing parameter control[23–25], microstructural impact[6,12,26–28], post processing[26], and mechanical properties[6,12,29]. Additional AM work using the powder bed fusion (PBF) process have also been performed, concentrating on microstructural characterization and the impact of hot isostatic pressing (HIP) on mechanical properties [30,31]. When the deposition process is scaled to these larger 3-dimensional structures, commonly encountered in AM processes, the governing process-structure-property relationships can change in unknown ways [32]. In addition, dilution of the weld composition combined with complex thermal cycles from the continuous layer-by-layer melting and remelting and heat inputs are factors that influence the solidification path and final microstructure of the material [27]. After AM structures are fabricated, they typically require an additional post processing step to remove porosity and stress relief the part. HIP, is currently the prominent technique used, however, its impact on the final solidification structure and resulting microstructure has not been studied [33].

Foster et al. investigated the impact of interlayer dwell times on the microstructural and mechanical properties using a laser-based DED process [34]. The study found that increasing the interlayer dwell time would decrease the substrate temperature, which therefore resulted in a finer microstructure. Along the height of the build, as the distance from the substrate increased, the secondary dendrite arm spacing (SDAS) was shown to coarsen. The coarsening of the dendrites resulted in a decrease in the Vickers microhardness measurements, shown in Figure 2.4 respectively. The interlayer dwell time and the height did not seem to impact the amount of secondary phase formation as there was a consistent measureable amount between 3.5 – 5.5 vol%.

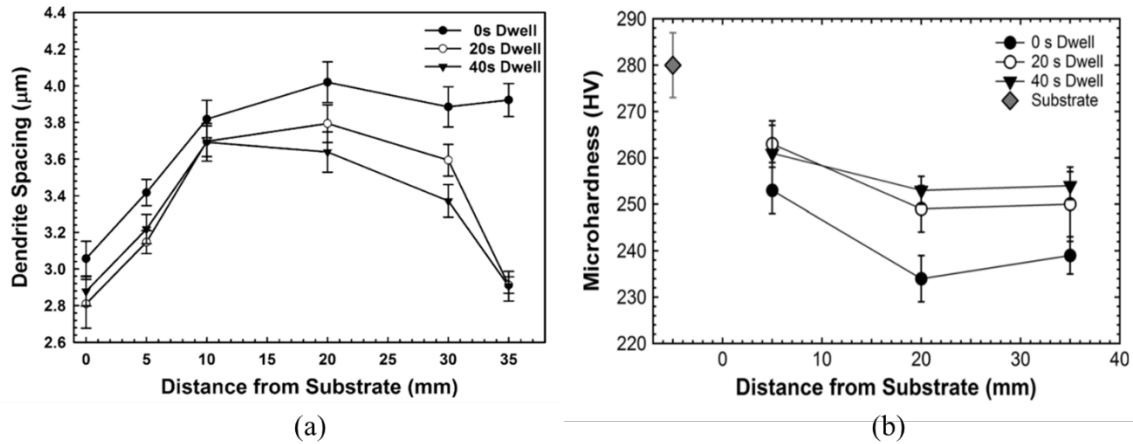


Figure 2.4: (a) Plot that describes along the build height, the dendrite arm coarsens; (b) plot that describes microhardness values decreased with height.

Murr et al. and Lass et al. recently investigated the microstructure for structures made using laser PBF, which were also heat treated [6,35]. These two studies characterized the secondary phase formation either as Ni_3Nb and/or Laves phase. In addition after a HIP treatment, Murr et al. reported a decrease in the strength and an increase in ductility. The HIP treatment homogenized the matrix and saw NbCr_2 Laves phase distributed throughout the grain structure.

Lass et al. built off of the work done by Murr et al. and characterized the secondary phase after stress relieving the components as Ni_3Nb δ -phase. Interdendritic regions where high concentrations of Nb and Mo existed enhanced the susceptibility of δ -phase to form. Because it is necessary to stress-relief AM components, it was recommended that a homogenization heat treatment should be included to ensure microstructural stability [35].

In past AM studies, the Fe content was held constant in the powder feedstock at levels either below [12,36,34,27,22,37] or above [6,26,29,25] 3 wt %. The resulting secondary phase constituents were characterized as NbCr_2 Laves phase, γ' (Ni_3Al), δ (Ni_3Nb), or a various carbide. However no work has been done in order to investigate how the alloying element compositions impact the resulting secondary phase and the properties of fabricated structures. In order to characterize the impact of Fe content on the resulting microstructure and mechanical properties of AM fabricated Inconel® 625 components, powder feedstocks with Fe contents 1 wt% and 4 wt%, respectively, are used.

Chapter 3

EXPERIMENTAL PROCEDURE

3.1 Powder Feedstock Characterization

Provided by the powder supplier, nitrogen atomized powder feedstocks¹ with a low Fe content (1 wt% Fe) and a high Fe content (4 wt% Fe) were sieved to a size range between -100/+270 sieve sizes for the low Fe and -120/+270 sieve sizes for the high Fe powder. Chemistries for the as received powder feedstock were measured at a certified testing laboratory² and are listed in Table 3.1. In addition to the increase in Fe composition there is a noticeable change in Mn, Si, and Ti content between the two powder feedstock powders. Standard characterization of the powder feedstock was also conducted and the results for these tests are listed in Table 3.2. The volume based particle-size distribution was measured using a Mastersizer 3000 (software version V3.62)³ laser diffraction particle size analyzer with a Hydro MV wet dispersion attachment. A small amount of dry powder was placed directly in small increments into the Hydro MV unit with a constant stirrer speed of 2390 RPM until an obscuration rate of 5% was achieved. The particle size distributions, including particle size at 10% (D₁₀), 50% (D₅₀), and 90% (D₉₀) of the volume distribution were calculated using refractive (1.86) and absorption (3.7) indices of dispersed droplets. Each powder feedstock was also characterized using traditional powder metallurgy techniques including Hall flow rate (ASTM B213)[38], apparent density (ASTM B212)[39], tap density (ASTM B527)[40], and angle of repose (ASTM C1444)[41].

3.2 Directed Energy Deposition Setup

A series of L-shaped builds, schematically shown in Figure 3.1, were fabricated using a laser based DED system on 150 x 150 x 13 mm Inconel® 625 substrates⁴. An IPG Photonics® YLR-12000 ytterbium fiber laser system that operates at a near-infrared wavelength between 1070 and 1080 nm, was used as the energy source. The laser was delivered through a 600 µm diameter fiber to a water-cooled copper reflective optics system, which consisted of a 49.5 mm diameter collimator with a 125 mm focal length lens and focusing optics with a focal length of 600 mm.

¹ Carpenter Powder Products (Bridgeville, PA)

² Luvak Laboratories (Boylston, MA)

³ Malvern Instruments (Westborough, MA)

⁴ American Special Metals (Pompano Beach, FL)

The powder feedstock was delivered through a Powder Feed Dynamics Mark XV Precision Powder Feeder to a custom coaxial, four nozzle powder delivery system, with each nozzle having an orifice size of 2 mm and located 10 mm above the deposition surface. At this stand-off distance, the measured defocused laser beam diameter was approximately 4 mm with a Gaussian energy density distribution confirmed using a PRIMES® Focus Monitor [43].

Table 3.1: Chemical compositions of low and high Fe content Inconel® 625. Standard composition is according to ASTM B705-05.[42]

Element	Alloy Compositions (wt %)				
		Low Fe		High Fe	
	Standard	Powder	Deposit	Powder	Deposit
Ni	> 58.0	64.8	64.06	61.3	60.62
Cr	20.0 – 23.0	21.0	21.59	21.3	21.46
Fe	< 5.0	1.02	1.07	4.34	4.14
Mo	8.0 – 10.0	8.73	8.83	8.70	8.96
Nb	3.15 – 4.15	3.43	3.47	3.83	4.11
Si	< 0.50	0.37	0.39	0.035	0.051
Mn	< 0.50	0.31	0.28	0.010	0.085
C	< 0.10	0.008	0.009	0.005	0.006
Ti	< 0.40	0.019	0.033	0.19	0.21

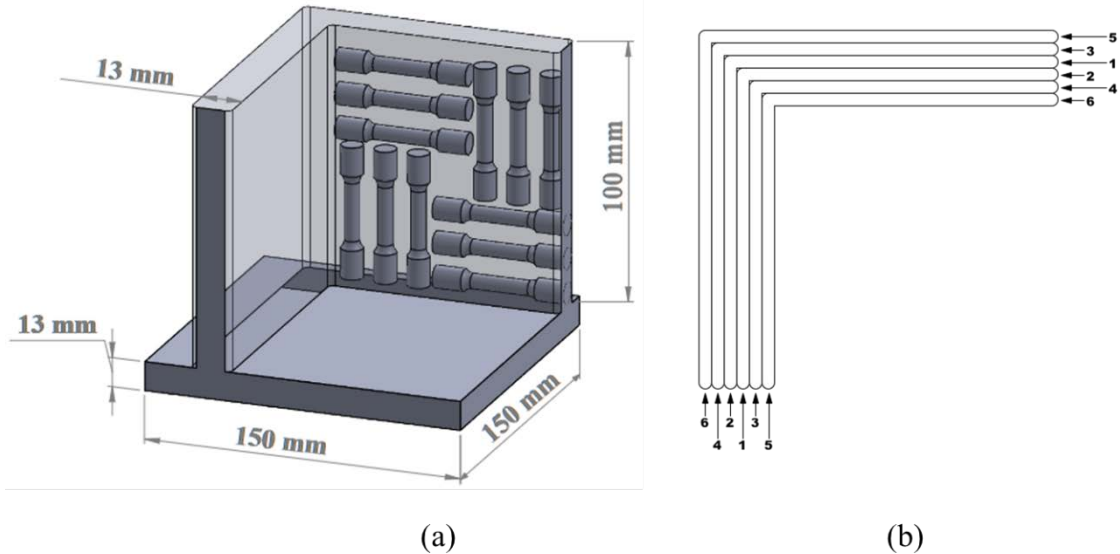


Figure 3.1: (a) Isometric view of the CAD model of the fabricated L shaped test structures via DED along with (b) the build paths for the L shaped structure. Also showing are the locations of where tensile specimens were extracted from in the fabricated structures. Longitudinal specimens are parallel to the substrate and transverse specimens are oriented perpendicularly.

3.3 Deposition Processing Parameters

All builds were fabricated using a laser power of 2000 W, a travel speed of 10.6 mm/s, and a mass flow rate of 14 g/min. A hatch spacing of 2.54 mm was used for the low Fe content builds and was adjusted to 2.29 mm for high Fe content builds to alleviate the formation of surface irregularities and defects. An argon gas flow rate of 2 L/min was used to deliver the powder and additional argon shielding gas was coaxially delivered along the laser path. During the fabrication of the L-shaped structures, successive layers were deposited in an alternating pattern [44], as shown in Figure 3.1b. Selected builds underwent a standard HIP treatment at a temperature of 1163 ± 25 °C and a pressure of 101 MPa for 14400 seconds⁵. All builds were inspected for internal pores and defects using a X-ray Computed Tomography (CT) system (GE, phoenix v|tome|x m 300) equipped with a 300 kV micro-focus x-ray source at a potential of 200 kV and current of 50 μ A, with a voxel size of 100 μ m. Shown in Figure 3.2, after an X-ray CT scan was performed, an image of the L-structures is developed based upon rendering the scanned data. Once an identified volume was determined a porosity analysis was conducted in order to detect observable defects shown in Figure 3.2b. Based upon the observable defects a volume percent was able to be calculated.

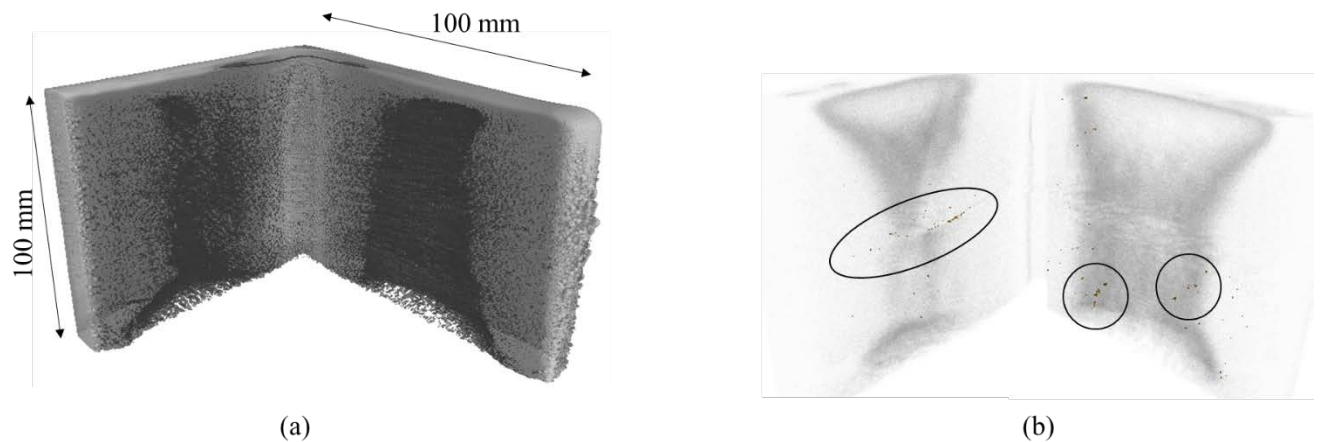


Figure 3.2: A representative X-ray CT scan of a fabricated structure (a) before and (b) after conducting a porosity analysis to measure the defects levels in the as deposited condition. Noted in the porosity analysis scan are where defects were detected.

⁵ Bodycote (Andover, MA)

Table 3.2: Powder measurement results from the PSD results and additional powder characterization.

	Low Fe	High Fe
Particle Size Distribution (μm)		
D_{10}	58.44 ± 0.67	45.18 ± 0.82
D_{50}	94.96 ± 0.09	69.92 ± 0.29
D_{90}	153.20 ± 0.45	108.0 ± 0
Powder Characterization		
Flow Rate, FR_H (sec)	13.9 ± 0	13.5 ± 0.06
Apparent Density (g/cm^3)	4.63 ± 0.01	4.35 ± 0
Tap Density (g/cm^3)	5.3 ± 0.01	5.1 ± 0
Angle of Repose (degrees)	27	30.5

3.4 Microstructural Characterization

Microstructural characterization was conducted to provide initial insight into the build quality. After solidification operations are conducted on Inconel® 625 samples, the resulting microstructure depends on the solidification mode, which is characteristic of the cooling rates and temperature gradients during deposition. Important inferences that can be made from the microstructure include the thermal conditions experienced along the build height, the secondary phase size and distribution throughout the microstructure, and the localized strength of the structure through microhardness measurements. To investigate the role of height, samples were sub-sectioned at different distances away from the substrate and characterization was conducted throughout the entire extracted sample.

3.4.1 Metallurgical Preparation

After fabrication and post processing, samples approximately 25 x 13 x 13 mm in size were extracted along the build height and used for metallurgical characterization. Samples were ground with a series of silicon carbide papers up to P2000 ISO grit size, polished with 3 μm and 1 μm polycrystalline diamond suspension, and had a finish polish with 0.05 μm colloidal silica for 480 seconds. Samples were immersed in a 10% oxalic solution and electrolytically etched at a potential of 2V for a time of 5s to prepare samples for optical microscopy using a Nikon Epiphot microscope.

3.4.2 Secondary Dendrite Arm Spacing

Solidification structures of Inconel® 625, obtained optically using microscopy and shown in Figure 3.3 contain primary and secondary dendrite arms and secondary phases. The secondary dendrite arm spacing (SDAS) is an important solidification feature, which can be quantitatively correlated with cooling rates related to solidification [45]. SDAS was measured by locating at least five consecutive secondary dendrite arms and measuring the spacing between them. A minimum of 32 intercepted secondary dendrites arms were measured along the build height using ImageJ® (National Institutes of Health, Bethesda Maryland) to determine peak gray values which signified the center of each secondary dendrite arm. The length of the line across the secondary dendrite arms was determined by using the image pixels to micron conversion feature within the software [34]. Once the length of the line and the number of dendrites the line intercepted was determined, the SDAS, λ_2 , was calculated using equation 1, where L is the length of the line and n is the number of intercepted dendrites.

$$\lambda_2 = \frac{L}{(n - 1)} \quad (1)$$

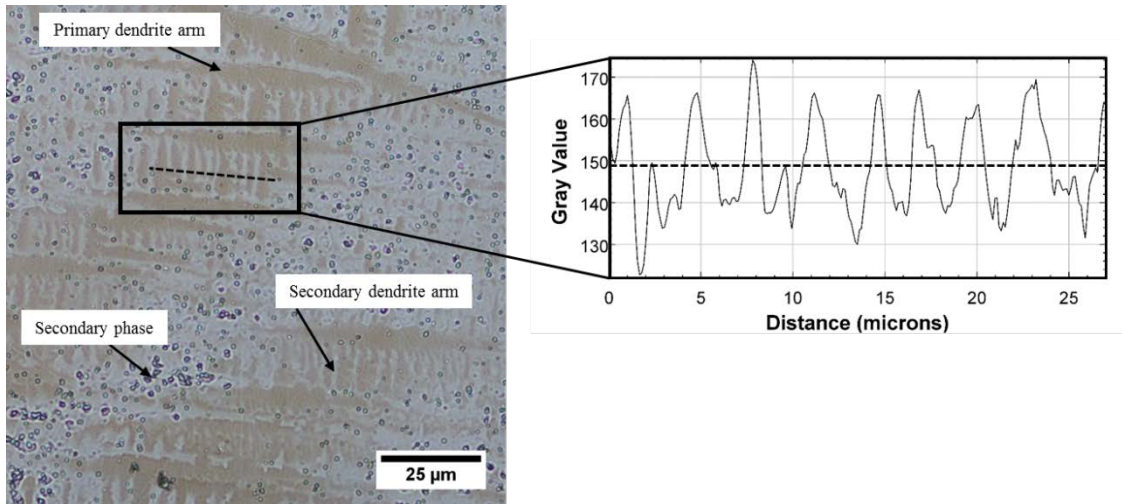


Figure 3.3: Image analysis was used to measure the SDAS depicted above. The peaks for the plot profile, where the y-axis is gray value, denote the interdendritic regions. Also denoted in the figure are constituents that form upon solidification

3.4.3 Secondary Phase Volume Fraction Analysis

Analysis of the optical microscopy image was also used to determine the average secondary phase particle size and volume fraction. The threshold feature in ImageJ® was used to calculate

the size and volume fraction of the secondary phases depicted in Figure 3.4. In the threshold process, a standard optical micrograph is converted to an 8-bit, black and white image. The microstructural features are then filtered so that only secondary phase particles remain. Once a threshold limit has been set, the size of each particle and volume fraction are calculated using a grey scale color analysis.

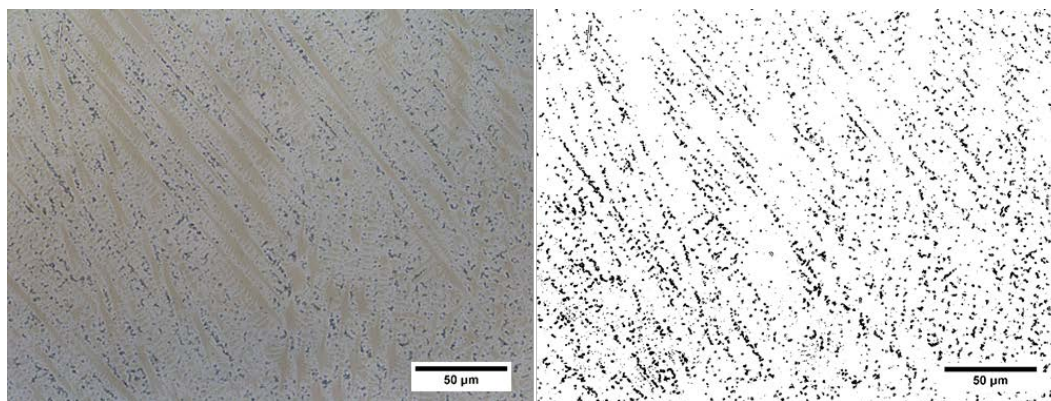


Figure 3.4: Image analysis was used to measure the average secondary phase particle size. The threshold technique was used to remove certain features and then determine the size of all the dark colored particles.

3.5 Elemental Composition Measurements

To identify small microstructural features and investigate the segregation of elements of the solidification structures, a scanning electron microscope (SEM) (FEI, Quanta 200) equipped with an energy dispersive X-ray spectroscopy (EDS) detector was used. An accelerating voltage of 20 kV, working distance of 10 mm, and a spot size of 6.8 mm was used to obtain the necessary high signal count needed for quality EDS scans. The EDS composition maps were used to show the microsegregation of Nb and Mo to the interdendritic regions in the as deposited condition and the formation of precipitates in the HIP condition.

To verify the measurements of the elemental composition of the secondary phase constituents, point analyses and line scans were conducted using an electron probe micro-analyzer (EPMA). This supplementary analysis of the constituents could possibly allow for a more in depth characterization of whether Laves phase or carbides was the predominately forming species. The microprobe was operated at an accelerating voltage of 20 kV and a beam current of 20 nA. Elemental standards of SiC, Ti, Nb₂O₅, Inconel® 600, and Mo were used to identify Ni, Cr, Fe,

Nb, Mo, C, Si, and Ti composition in the Inconel® 625 alloy microstructure. K_{α} lines were used for Ni, Fe, Cr, Ti, Si and C while L_{α} lines were used for Nb and Mo.

3.6 Grain Size Measurements

To analyze grain size and morphology of the fabricated Inconel® 625 samples, electron backscatter diffraction (EBSD) was performed using a FEI Helios NanoLab 660 FEG-SEM coupled with an Oxford Instruments NordlysMax² detector. A 70° pre-tilt specimen holder was used, and the sample was oriented towards the detector. EBSD specimens required a final polish using a Buehler VibroMet Vibratory Polisher with 0.05 μm colloidal silica for 12 hours.

Following metallographic preparation, in order to quantify the findings of the EBSD scans, imageJ® was used to determine the average grain size area, major axis, minor axis, and aspect ratio, which is shown in Figure 3.5. The elliptical tool was utilized to make approximations of the columnar grain morphology. Based on the measurement settings of the software, the area, fit ellipse, shape descriptors, centroid, and center of mass identifier were all reported. The display label setting, which numbered the grains as measurements were taken was used to avoid duplicates. Averages and standard deviations were calculated and reported in the results and discussion chapter.

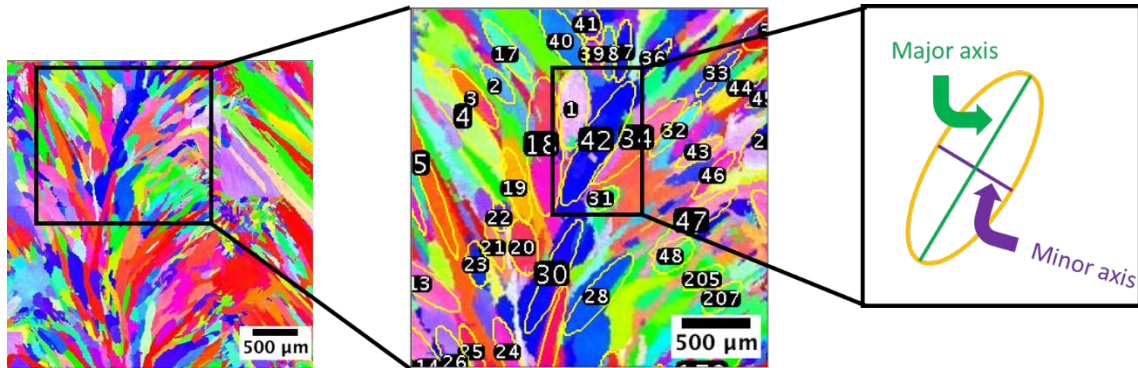


Figure 3.5: Schematic diagram describing how grain size was determined from the EBSD scans. Also identified in the figure are the major and minor axes.

3.7 Mechanical Property Characterization

Microhardness measurements generally correspond to the same general trends observed in the microstructure. Testing was also conducted along the build height using a Leco® M-400-G1

Vickers hardness tester. Hardness indentations were spaced 3 mm horizontally and vertically to avoid any interactions between measurements. An applied load of 300 g with a dwell time of 5s was used for all indentations. The average and standard deviation from the measurements taken at each height are reported.

Room temperature mechanical testing, with a strain rate of 0.3 s^{-1} , was conducted in accordance with ASTM E8[46] at a certified testing laboratory⁶. Tensile specimens, shown in Figure 3.6, which met ASTM E8 standards[46] with a gauge diameter of 6.35 mm and a gauge length of 25.4 mm were extracted from selected locations and at different orientations from the builds using electrical discharge machining (EDM). Figure 3.7 provides location specific information on where tensile specimens were extracted. The 0.2% offset yield strength and tensile strength were obtained from the resulting stress-strain curves, and the elongation was determined by measuring the gage length before and after failure.

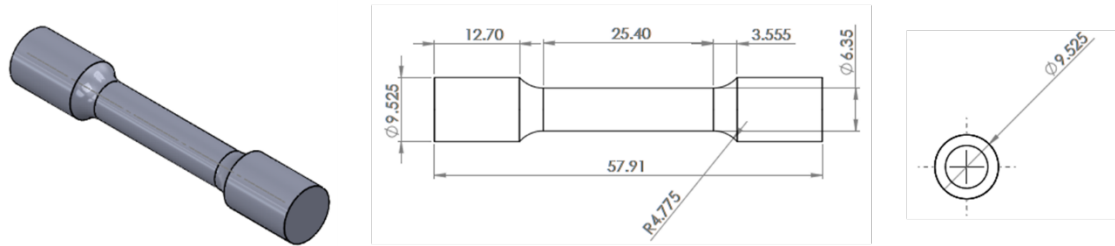


Figure 3.6: Representative tensile specimen that was extracted from the fabricated structures and used for mechanical testing. All measurements are in mm.

⁶ Westmoreland Mechanical Testing & Research, Inc. (Youngstown, PA)

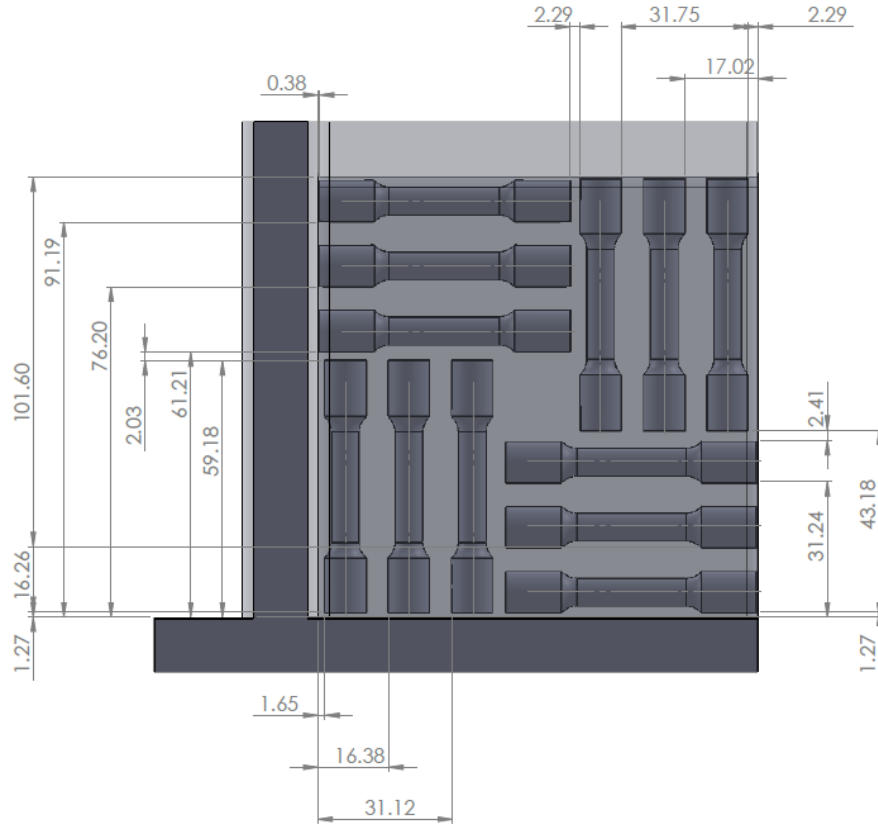


Figure 3.7: Schematic diagram detailing the location at which tensile specimens were extracted. All measurements are in mm.

3.7.1 Strain Hardening Coefficient Measurements

In order to calculate the strain hardening exponent [47], the engineering stress (σ_e) and strain (ϵ_e) data was converted to the true stress (σ_t) and strain (ϵ_t) data by using equations 2 and 3.

$$\epsilon_t = \ln(1 + \epsilon_e) \quad (2)$$

$$\sigma_t = \sigma_e(1 + \epsilon_e) \quad (3)$$

True stress vs. elastic stress was plotted and then a power trendline was fitted to the data. The plot was modeled in the form of an equation seen in equation 4, which is the stain hardening power-law equation:

$$\sigma_t = K\epsilon_p^n \quad (4)$$

where σ_t is true stress, ε_p is plastic strain, K is the strength coefficient of the material, and n is the strain hardening exponent. From the equation the n-value can be determined. Twelve measurements were made for each recorded strain hardening value.

Chapter 4

ANALYSIS OF STRUCTURES IN THE AS DEPOSITED CONDITION

Two powder feedstock materials with Fe composition at the 1wt% and 4 wt% are initially characterized. Subsequently, the feedstock material was utilized for deposition. Three dimensional, free-form structures are fabricated and characterized in the as deposited condition. Analysis of microstructures, mechanical properties, and solute segregation is presented in this chapter. Characterization of the as deposited condition provides a baseline for comparisons made in the following chapter on the role of hot isostatic pressing (HIP) on the fabricated structures.

4.1 Powder Feedstock Characterization

Powder feedstocks that meet the chemistry specifications for Inconel® 625 are typically considered equivalent and expected to behave in similar ways. However, the wide range of allowable compositions in the standards governing this alloy system can have unexpected effects on the powder feedstock and the resulting build as listed in Table 3.1. For example, a change in Fe content from 1 wt% to 4 wt% resulted in differences in the morphology of the powder feedstocks, as shown in Figure 4.1. The low Fe content powder was generally spherical in shape and free of satellites, while the high Fe content powder displayed a large number of satellites and fines, which resulted in an increase in the appearance of particle roughness.

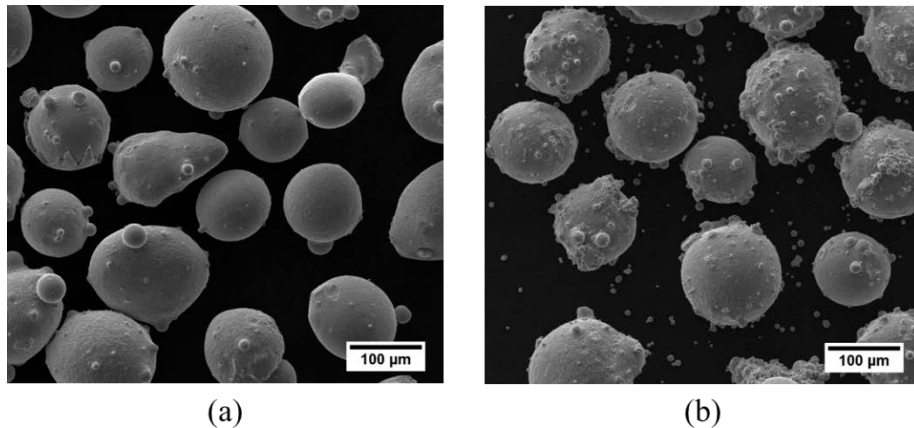


Figure 4.1: SEM micrograph of the (a) low and (b) high Fe Inconel® 625 nitrogen atomized powder. High Fe content powder particles show presence of satellite formation.

Particle size distribution (PSD) curves are shown in Figure 4.2, and the resulting D_{10} , D_{50} , and D_{90} are listed in Table 3.2. Low and high Fe content powder feedstocks were sieved at slightly different ranges, and this difference is portrayed by the shift in the Gaussian distribution in Figure

4.2 and resulting PSD values. Low Fe content powder feedstock had a wider distribution and a larger average (D_{50}) of $95.0 \pm 0.1 \mu\text{m}$, compared to $69.9 \pm 0.3 \mu\text{m}$ for high Fe content powder feedstock. The larger mean particle size for the low Fe content powder feedstock did not impact the flowability, apparent density, and tap density, with each powder feedstock displaying similar values. The angle of repose, however, differed between the low and high Fe content powder feedstocks. Low Fe content had an angle of repose value of 27° , compared to the high Fe content angle of repose value of 30.5° . The change in angle of repose value is attributed the change in size of the powder feedstock particles and also the amount of fines each powder feedstock contained [48]. High Fe content powder feedstock contains more fines, as shown in the SEM image in Figure 4.1. As a consequence, the interparticle friction increases [49], which affects the flowability of the powder particles and produces higher angle of repose values.

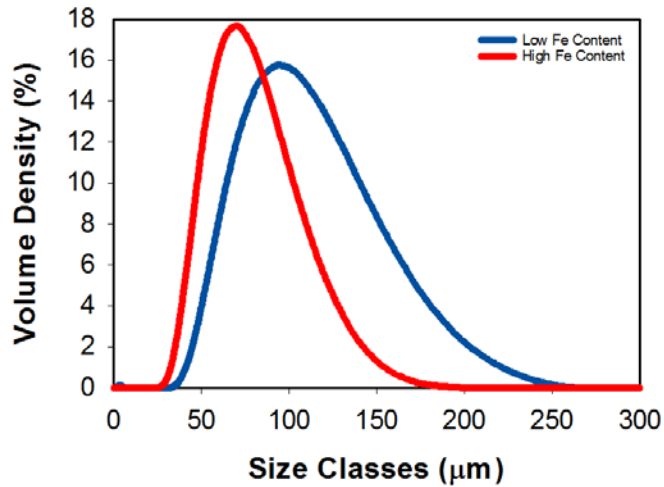


Figure 4.2: Particle size distribution curves of low and high Fe powder feedstock material detailing the difference in size and spread between low and high Fe feedstock materials

4.2 Analysis of Fabricated Structures

Each powder feedstock was then used to fabricate a series of L-shaped structures in order to evaluate the impact of changes in powder feedstock Fe composition on the resulting as deposited build characteristics. From a processing perspective, the volume fraction of defects, typically resulting from lack of fusion, is an important consideration. CT X-ray scans were used to report porosity levels below 0.005 vol % for both powder feedstocks. All analyzed defects were randomly distributed, indicative of lack of fusion, and had a calculated volume of less 0.2 mm^3 seen in Figure 3.2 [32].

Microstructural analysis of low and high Fe content builds displayed similar structures comprised of primary and secondary dendrites and secondary phases, as shown in Figure 4.3 and Figure 4.4. Overall, there was very little change in the microstructural appearance between the builds even at higher magnification, as shown in Figure 4.3b and Figure 4.4b for the low and high Fe content builds, respectively.

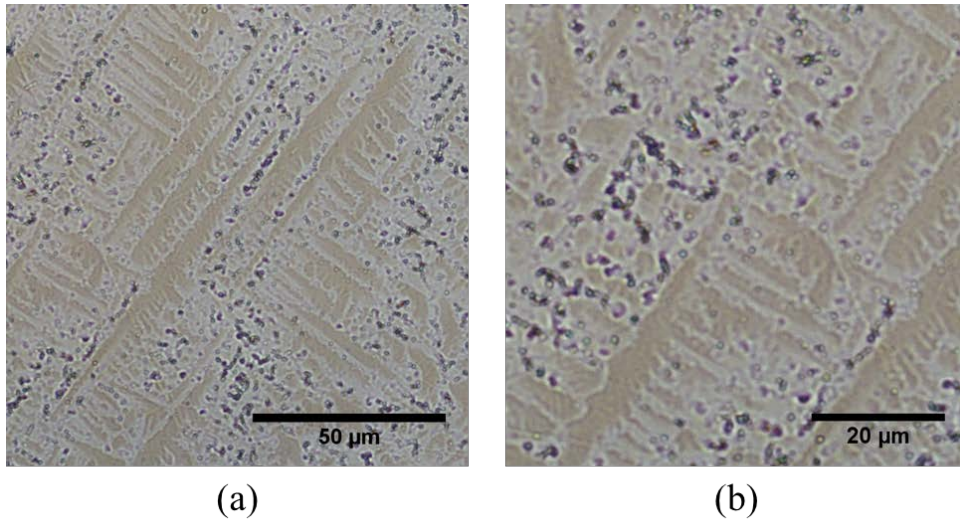


Figure 4.3: Optical microscopy images of low Fe, as deposited. (b) is a magnified micrograph of a representative location to depict the secondary phase formation.

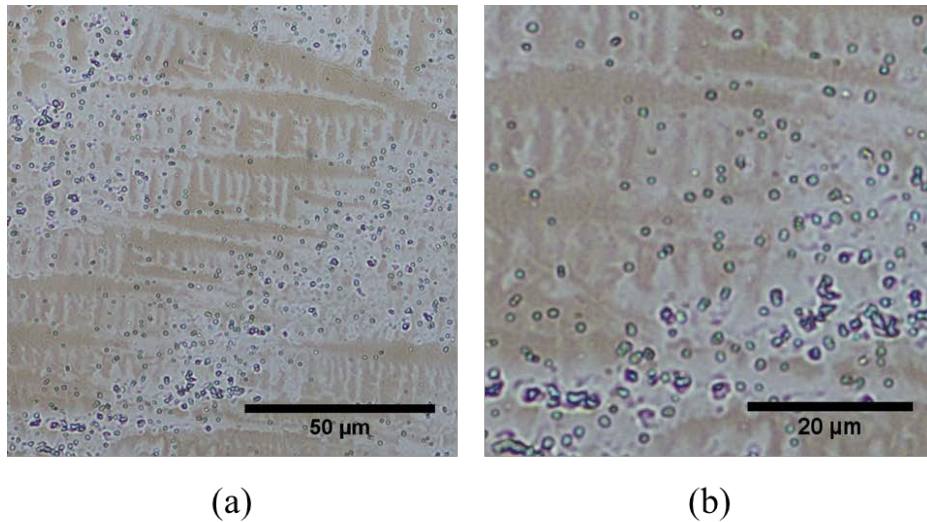


Figure 4.4: Optical microscopy images of high Fe, as deposited. (b) is a magnified micrograph of a representative location to depict the secondary phase formation

SDAS has been quantitatively correlated with cooling rates for Ni base alloys and can offer location specific information on how the cooling rate evolved throughout the height of the build

[45]. SDAS measurements were also made for each build and plotted as a function of build height, as shown in Figure 4.5. There was no change in SDAS between Fe contents and with height with the average SDAS measurements. For low Fe content samples, SDAS values of $4.43 \pm 0.22 \mu\text{m}$ were measure, while for high Fe content samples these values were approximately $4.12 \pm 0.38 \mu\text{m}$. The similar SDAS measurements indicate that both samples experienced similar thermal conditions during AM fabrication.

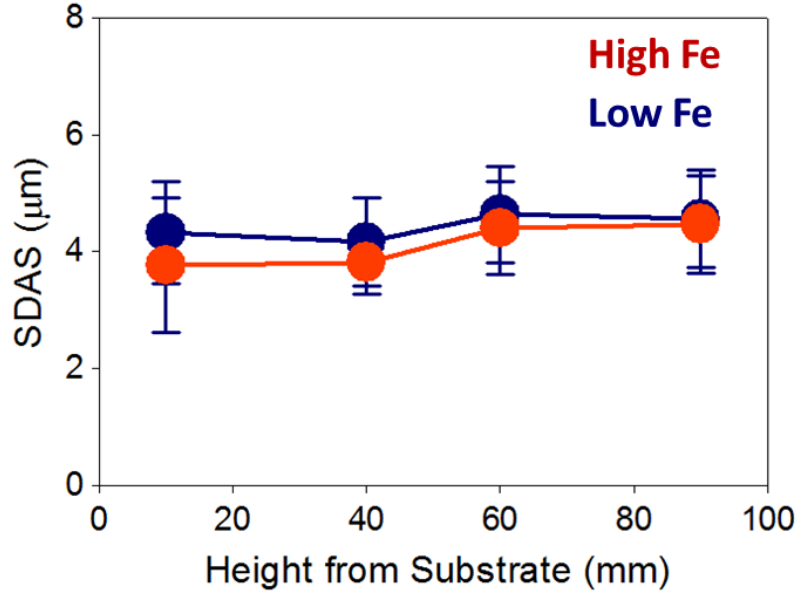


Figure 4.5: SDAS measurements for low and high Fe content samples in the as deposited condition.

Microhardness measurements for low and high Fe content builds are plotted in Figure 4.6 as a function of height. These results generally expand on what is observed microstructurally through the SDAS measurement, since much of the strength of Inconel® 625 is derived from its solidification structure [34]. In the as deposited condition, the average Vickers microhardness value for the low Fe content builds is $257 \pm 9 \text{ HV}$ and for the high Fe content builds is $258 \pm 3 \text{ HV}$. No location dependence is observed in measurements made at different heights. Finer SDAS will have higher microhardness values, but because the SDAS is similar between low and high Fe content samples, the microhardness measurements are similar as well.

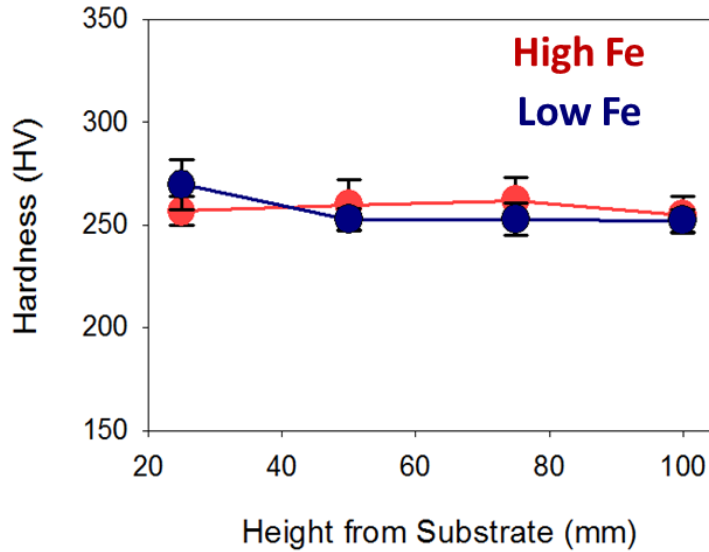


Figure 4.6: Microhardness measurements of low and high Fe content samples in the as deposited build condition

The similarities in microstructure and microhardness measurements for the low and high Fe contents were expected to lead to similarities in mechanical properties. Static mechanical testing was conducted on specimens extracted from the build at various heights and orientations, as shown in Figure 3.1. Results of these mechanical tests are listed in Table 4.1. In the as deposited condition, the Fe content had a significant impact on the mechanical properties. Low Fe content specimens exhibited higher yield and tensile strengths but lower elongations. Low Fe content specimens, for example, had an average yield strength of $520 \text{ MPa} \pm 12 \text{ MPa}$, compared to an average yield strength of $450 \text{ MPa} \pm 27 \text{ MPa}$ for high Fe content specimens. While low Fe content specimens had greater strengths, high Fe content specimens exhibited an average elongation value of $44 \pm 9 \%$ compared to an average of $36 \pm 5 \%$ for the low Fe content samples. Mechanical testing results did not show a dependence on height or orientation.

A comparison between the engineering and true stress-strain curves in Figure 4.7 revealed that as high Fe content tensile specimens elongated, the slope of the line from the proportional limit to UTS increased from 0.33 ± 0.04 to 0.38 ± 0.02 . The larger strain hardening exponent allowed high Fe content specimens to reach a UTS value of $753 \text{ MPa} \pm 25 \text{ MPa}$. The strain hardening exponent was greater in the as deposited high Fe content specimens, and as a consequence tightened the range between the ultimate tensile strength (UTS) values for the low and high Fe content specimens.

Table 4.1: Mechanical property results for low and high Fe, as deposited and HIP, Inconel® 625 tensile specimens. Strain hardening exponent values are calculated and shown as well. Standard values are from Special Metals certification.[2]

Fe Content & Build Condition	Orientation	Number of Tensile Specimens Tested	Yield Strength (MPa)	UTS (MPa)	Elongation (%)	Strain Hardening Exponent
Low Fe As deposited	Longitudinal	6	531 ± 7	874 ± 25	32 ± 3	0.33 ± 0.04
	Transverse	6	508 ± 10	846 ± 24	40 ± 4	
	Average	12	520 ± 12	860 ± 27	36 ± 5	
HIP	Longitudinal	6	394 ± 17	841 ± 25	42 ± 4	0.40 ± 0.01
	Transverse	6	402 ± 15	848 ± 29	46 ± 4	
	Average	12	398 ± 16	845 ± 26	44 ± 4	
High Fe As deposited	Longitudinal	6	460 ± 35	763 ± 27	40 ± 7	0.38 ± 0.02
	Transverse	6	439 ± 6	743 ± 27	49 ± 8	
	Average	12	450 ± 27	753 ± 25	44 ± 9	
HIP	Longitudinal	6	383 ± 17	781 ± 28	48 ± 4	0.42 ± 0.01
	Transverse	6	387 ± 6	774 ± 16	55 ± 3	
	Average	12	385 ± 12	778 ± 22	51 ± 5	
Standard	As-rolled		414 – 758	827 - 1103	30 – 60	
	Annealed		414 - 655	827 - 1034	30 - 60	

While the observed microstructures for both sets of builds with different Fe contents were similar, these difference in mechanical properties can be attributed to differences with the secondary phase formation or grain size. It is known that secondary phases, such as Laves phase and carbides, are also observed in AM, cladding, and welding processes using Inconel® 625 [18]. Both solidification structures had blocky, irregularly shaped morphologies for the secondary phase constituents in the as deposited condition. The overall average measured secondary phase particle size and volume fractions are shown in Figure 4.8, and there was no indication height influenced particle size or volume fraction. The average amount of secondary phase in low Fe content was 4.9 ± 0.4 % compared to 3.9 ± 0.5 % for high Fe content. In terms of particle size, the low Fe content samples reported an average particle size of 0.88 ± 0.21 μm and high Fe content samples had a size of 0.66 ± 0.29 μm . Previous solidification studies of Inconel® 625 suggested that increased amounts of Fe promoted secondary phase, specifically, Laves phase formation [8,14]. However in this study there is no strong supporting evidence for such a connection.

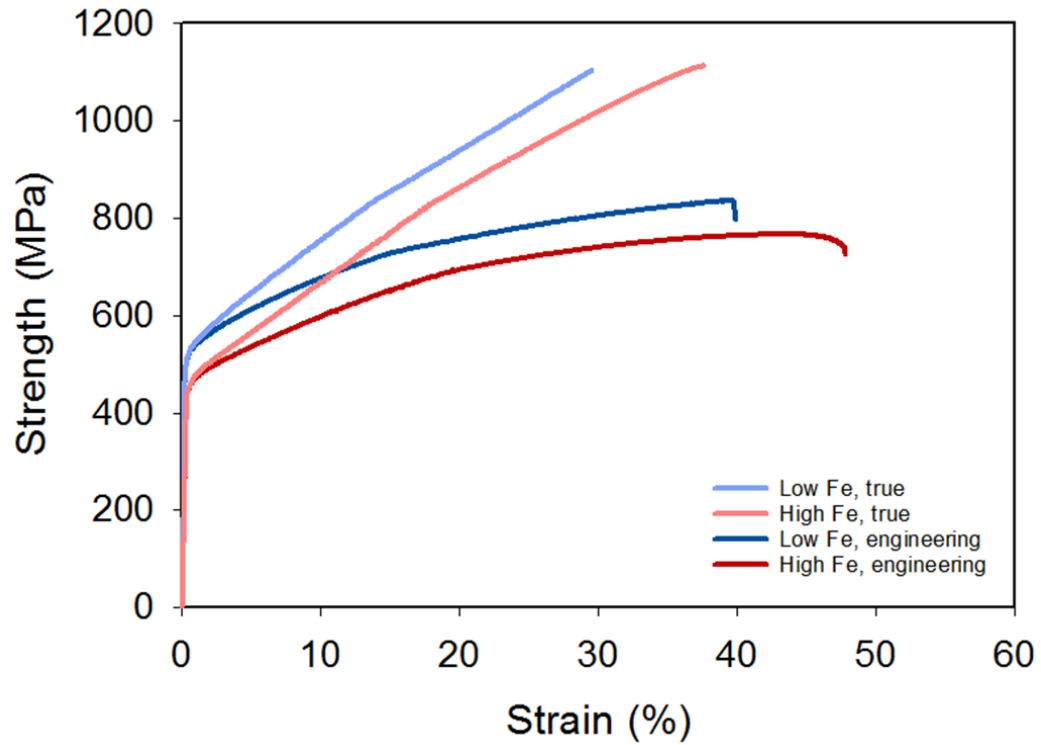


Figure 4.7: Representative engineering stress-strain and true stress-strain curves comparing the impact of Fe content on the strain hardening of Inconel® 625 during tensile testing.

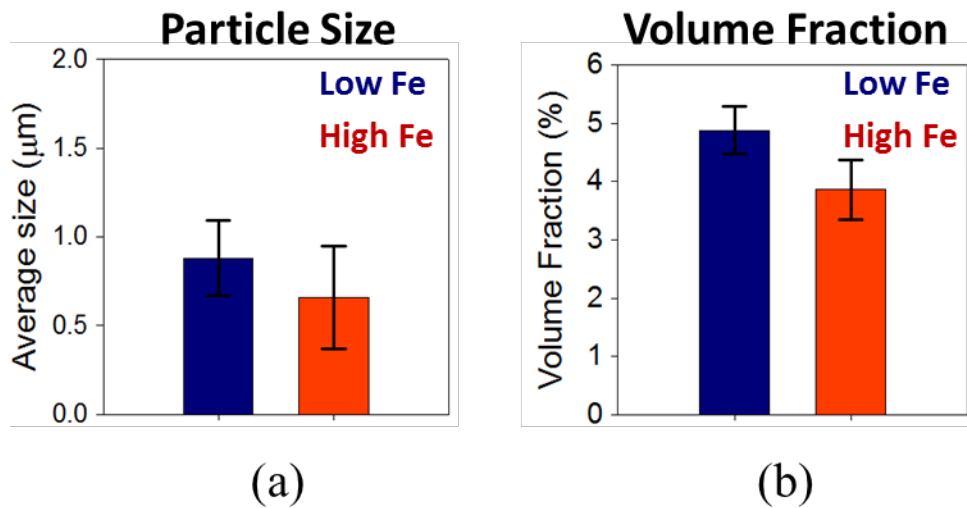


Figure 4.8: Graphs displaying the similar amounts of secondary phase (a) particle size and (b) volume fraction for low and high Fe content samples.

A more in depth analysis to determine any differences in secondary phase formation was conducted using backscattered-electron (BSE) imaging along with EDS maps of low and high Fe content samples, as shown in Figure 4.9. Interdendritic regions for both low and high Fe content samples were significantly enriched with Mo and Nb. Randomly dispersed throughout the matrix are remnants of additional alloying elements such as Si in low Fe and Ti in high Fe content samples. In Figure 4.9b, the black dots are indicative of Ti rich regions as seen in the EDS elemental map for Ti. However, similar segregation patterns are observed and do not appear to be responsible for these differences in mechanical properties.

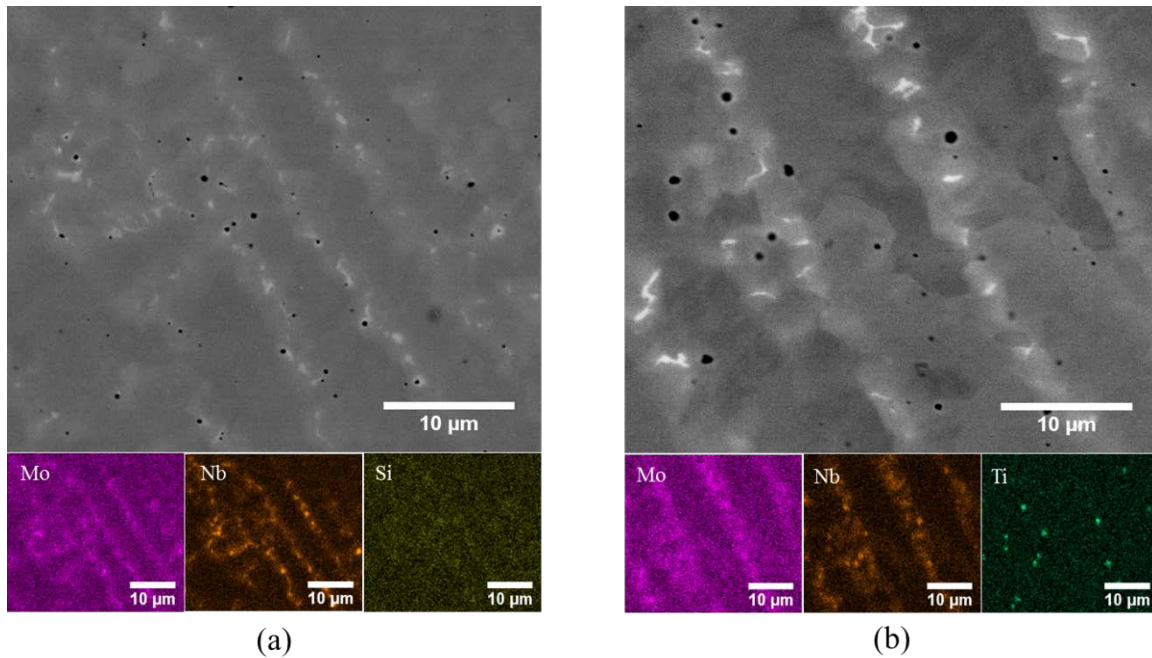
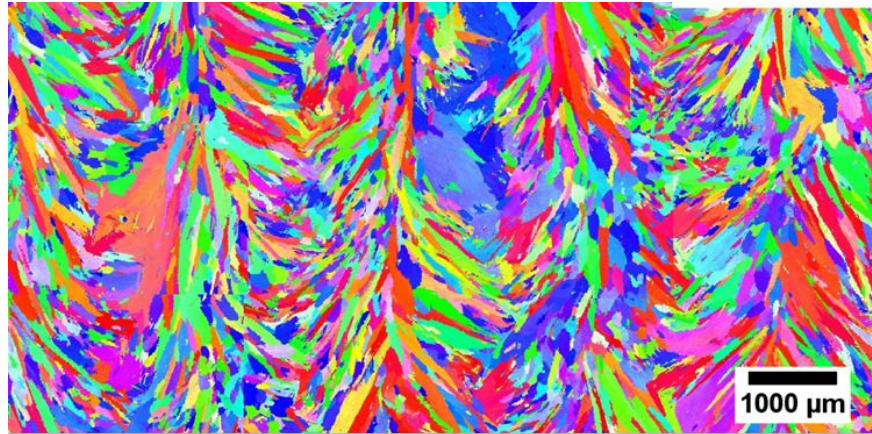


Figure 4.9: EDS maps of (a) low Fe and (b) high Fe in the as deposited detailing the secondary formation enriched in Mo and Nb.

Grain size, on the other hand, presented a clear link with the differences in mechanical properties. The impact of Fe content on the size and morphology of the grains was investigated using EBSD. Figure 4.10 shows representative grain structures in low and high Fe content samples extracted from a location approximately 80 mm above the substrate, where a single location was investigated. There are distinct differences in grain size between the Fe compositions. Using the ellipsoid approximation technique, the low Fe content samples had an average grain area of $39,600 \mu\text{m}^2$, while the high Fe content samples had an average grain area of $441,500 \mu\text{m}^2$. The

average area, major and minor axis, and aspect ratio of the as deposited grains are listed in Table 4.2.



(a)



(b)

Figure 4.10: EBSD images in the as deposited condition of (a) low Fe and (b) high Fe.

Table 4.2: Statistical information for grain size and morphology for low and high Fe content builds

	Low Fe		High Fe	
	As deposited	HIP	As deposited	HIP
Grain size and morphology measurements				
Mean of grain area (μm^2)	39600	37000	441500	422900
Average aspect ratio	4.4 ± 2.6	4.0 ± 2.2	5.5 ± 4.6	7.5 ± 5.8
a (μm)	429	390	1085	1468
b (μm)	108	106	280	254

The aspect ratio is the ratio of the major axis, a, to the minor axis, b [50]. An aspect ratio of 1 would signify that the grain is equiaxed. Low Fe content samples had columnar grains that had an aspect ratio of 4.4 ± 2.6 and an average major axis average of 429 μm . High Fe content builds had a similar aspect ratio of 5.5 ± 4.6 with a major axis of 1085 μm . The difference in grain size is shown by the average grain size value. Low Fe content as deposited grains had an average size that was approximately ten times smaller than the average grain area in the high Fe content samples. Figure 4.10 distinctly shows that high Fe content samples resulted in larger grain sizes, which can be directly correlated with decreased strength and increased ductility in the as deposited condition. How the composition of the alloy impacted the resulting grain area is not entirely understood and more work into this relationship would need to be investigated.

4.3 Summary and Conclusions

Structures fabricated using two Inconel® 625 powder feedstock materials with Fe content at 1 wt% and 4 wt% were investigated using laser-based DED builds that were characterized in the as deposited condition. Standard metallographic preparation was completed and multiple characterization techniques were conducted in order to come up with the following conclusions.

- Initial microstructural characterization of the as deposited structure showed no change between Fe content. Once static tensile testing was conducted, differences in performance were discovered.

- Low Fe content specimens exhibited higher strengths while high Fe content specimen exhibited more ductility. Mechanical properties did not change with height or orientation as well.
- EDS elemental maps revealed upon solidification elements segregated to similar locations for both Fe content samples. Interdendritic regions were Nb and Mo rich while dendritic features were composed of Ni, Cr, and Fe.
- EBSD scans were done in order to investigate grain size. Scans showed that high Fe content samples had much larger grain size formation on the order of ten times larger than the resulting average size for low Fe content samples. As a result, it is hypothesized that grain size is the primary strengthening mechanism for as deposited structures.

Chapter 5

ANALYSIS OF STRUCTURES IN THE HOT ISOSTATIC PRESSED CONDITION

HIP is currently the post processing technique used to remove possible porosity formation during fabrication. Structures were microstructurally characterized and correlations between the mechanical properties, grain size formation, and precipitate formation are developed. In most cases, post-process HIP operations are shown to significantly alter the as deposited structure as well as the resulting tensile properties for AM components [51].

5.1 Characterization of Post Processed Structures

A post processing HIP step is primarily used on AM structures to reduce internal porosity and other process related defects, such as lack of fusion [33]. For a range of materials, mechanical properties of wall structures fabricated using a laser based DED process have been shown to decrease after HIP post processing [6,44,52,31]. This temperature treatment is sufficient to recrystallize and promote grain growth of the microstructure leading to distinct microstructural and mechanical property changes from measurements in the as deposited condition [6]. Selected Inconel® 625 builds fabricated here were also subjected to a standard HIP cycle. X-ray CT scanning after the HIP cycle displayed no detectable levels of porosity in the build, shown in Figure 5.1. The detected levels of defect were not observed after the fabricated L-structure was post-processed using the same scanning parameters.

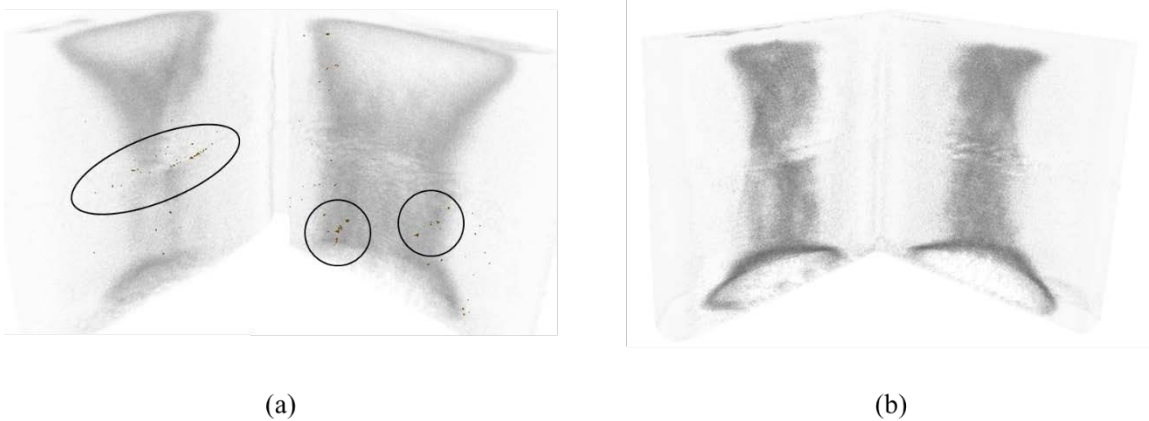


Figure 5.1: X-ray CT scans demonstrating the ability of a post processing HIP heat treatment to minimize defect level from the (a) as deposited condition to (b) HIP condition.

Representative microstructures of the post processed HIP structures are shown in Figure 5.2 and Figure 5.3, for the low Fe and high Fe content builds, respectively. The primary and secondary dendrite arms, prevalent in the solidification structure in the as deposited condition, are not observed in the HIP microstructure. Rather, secondary phases are readily distributed throughout the material matrix with no discernible sub-structure. Figure 5.4 shows the average particle size and volume fraction of the secondary phase. The particle size for low Fe content HIP structures grows in size from that observed in the as deposited condition to $1.36 \pm 0.12 \mu\text{m}$, while the particle size for the high Fe content HIP structures stays nearly the same at $0.56 \pm 0.08 \mu\text{m}$. The post processed volume fractions of measured secondary phase also show no significant difference with the as deposited condition, and the particles have spherical, irregular blocky shaped morphology with no distinguishable differences between the two Fe compositions.

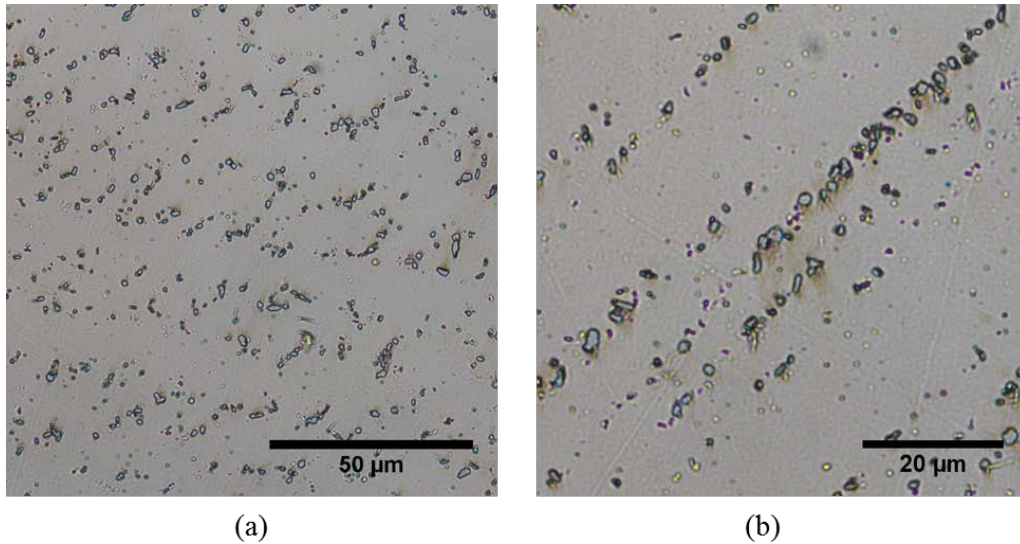


Figure 5.2: Optical microscopy image of (a) low Fe, HIP and (b) a magnified image of the secondary phase formation of the representative location within the same sample.

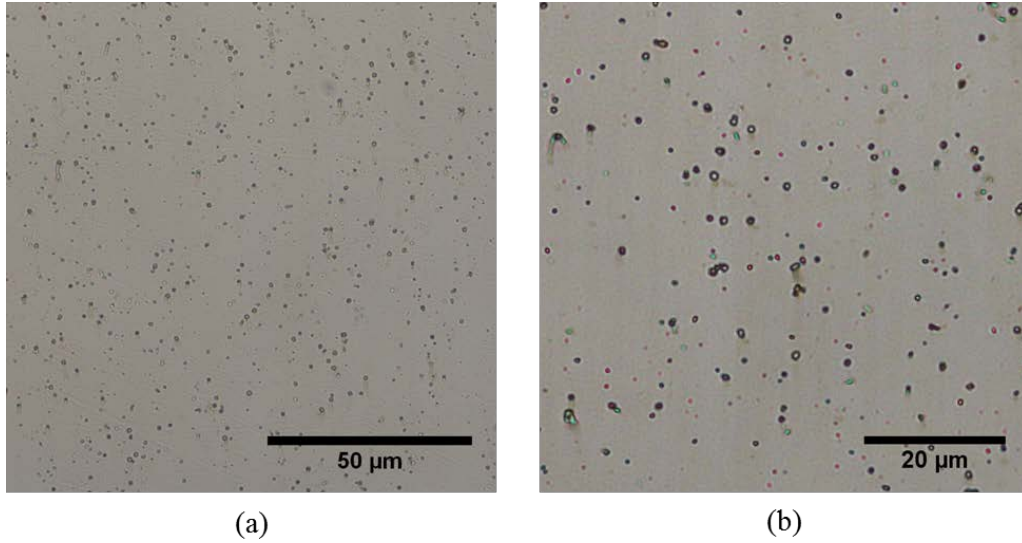


Figure 5.3: Optical microscopy image of (a) high Fe, HIP and (b) a magnified image of the secondary phase formation of the representative location within the same sample.

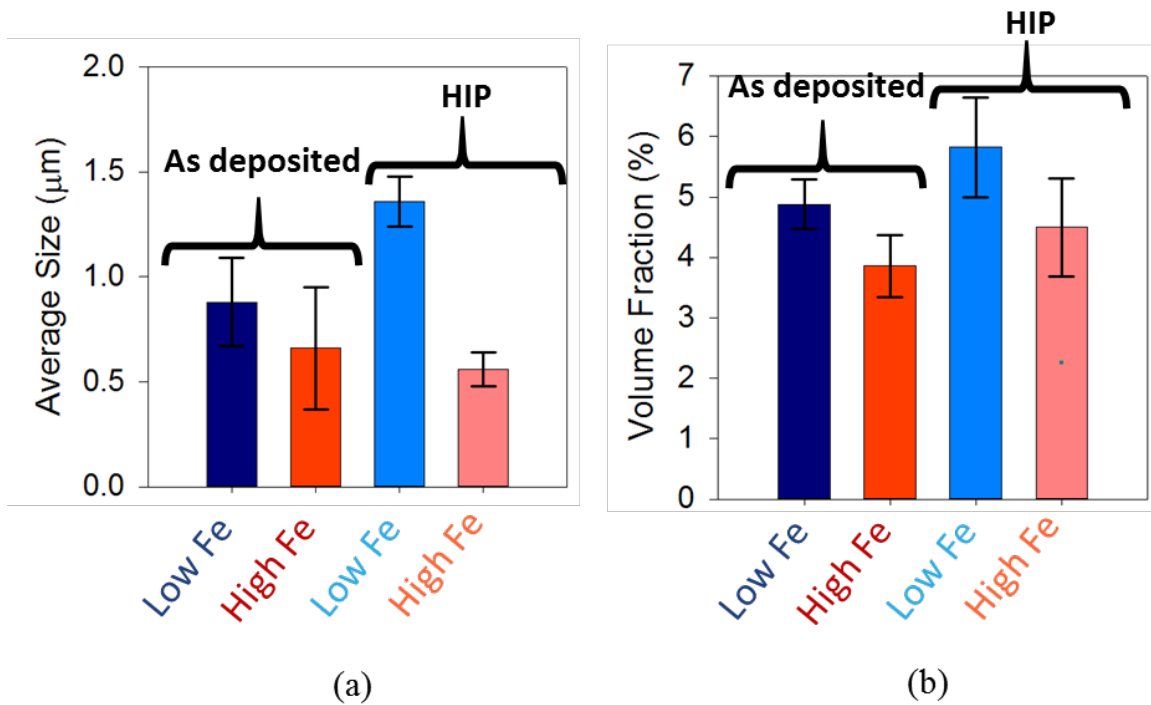


Figure 5.4: Secondary phase formation measurements of the (a) average size and (b) volume fraction.

Microhardness measurements were plotted as a function of height and shown in Figure 5.5. Measurements showed that there was no dependence on Fe content or height in the post processed condition. The average Vickers microhardness value for low Fe content was 224 ± 5 HV and for high Fe content was 220 ± 2 HV. The hardness values drastically decreased from the

averages of the as deposited condition shown in Figure 4.6 but remained consistent between the different Fe content feedstocks.

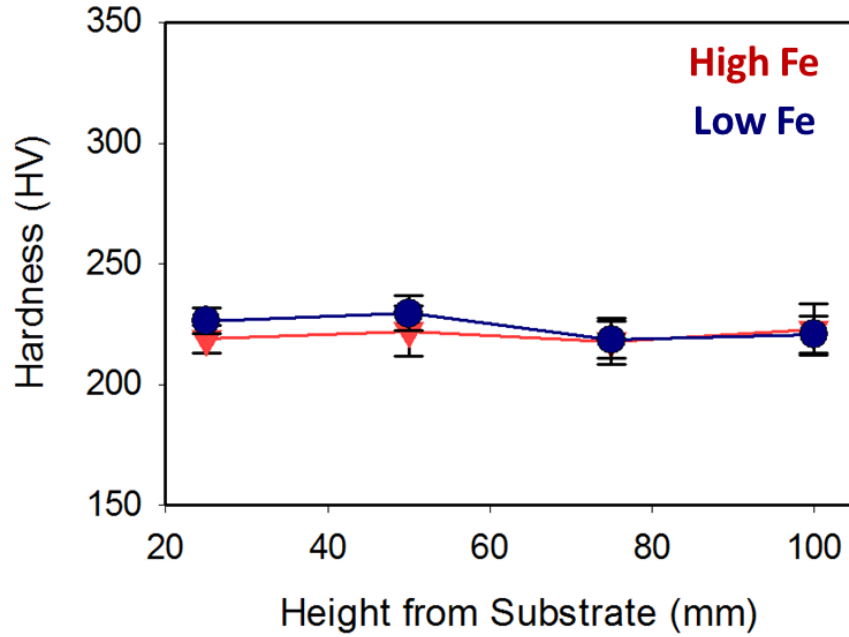


Figure 5.5: Microhardness measurements of low and high Fe content samples in the HIP condition.

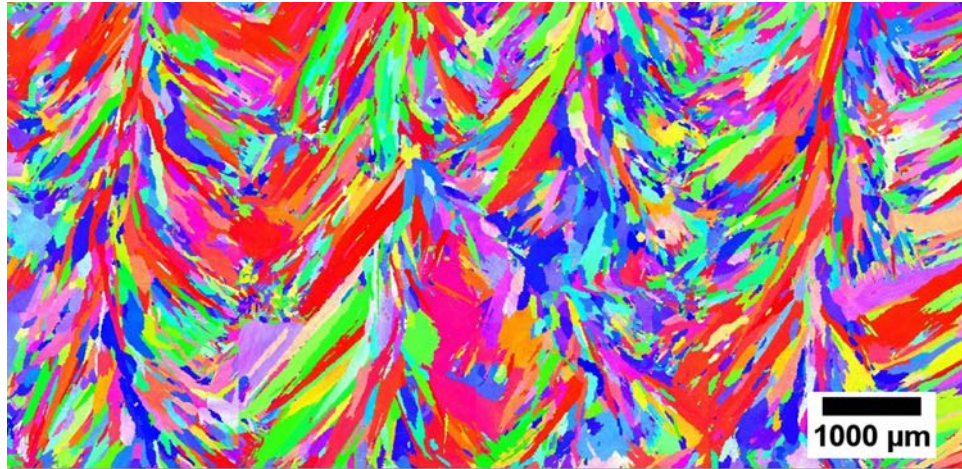
To further investigate the impact of post processing, mechanical testing was conducted on samples extracted from both the low Fe content and high Fe content structures. The mechanical property results are reported in Table 4.1. Similar to the microhardness measurements after the HIP cycle, yield strengths in the HIP condition significantly decreased from $520 \text{ MPa} \pm 12 \text{ MPa}$ to $398 \text{ MPa} \pm 16 \text{ MPa}$ for the low Fe content builds and from $450 \text{ MPa} \pm 27 \text{ MPa}$ to $385 \text{ MPa} \pm 12 \text{ MPa}$ for the high Fe content builds. The span which the specimens decreased from as deposited to HIP was 122 MPa for low Fe contents and 65 MPa for high Fe contents. An increase in ductility is exhibited by the HIP specimens with low Fe content elongation averages of $44 \pm 4 \%$ compared to high Fe content elongation averages of $51 \pm 5 \%$.

HIP specimens tended to achieve higher stress values for a given strain value, which was due to the larger strain hardening exponents, listed in Table 4.1[31,53]. As a result, higher UTS values, particularly for the high Fe content, were achieved by the HIP specimens because the strain hardening exponent from as deposited to HIP increased from 0.33 ± 0.04 to 0.40 ± 0.01 for low Fe content samples and from 0.38 ± 0.02 to 0.42 ± 0.01 for high Fe content samples. The UTS values

for high Fe tensile specimens were comparable in each condition with reported UTS values of 753 MPa \pm 25 MPa in the as deposited condition and 778 MPa \pm 22 MPa in the HIP condition. The large strain hardening exponent permitted higher strengths to be achieved as the specimens elongated.

It was shown in the as deposited condition that Fe content influenced the grain size, which impacted the mechanical properties. Similar to the as deposited EBSD scans in Figure 4.10, columnar grains were also seen in the HIP condition, as shown in Figure 5.6. The average aspect ratio for low Fe content samples was 4.0 ± 2.2 with a major axis of 390 μm , and the average aspect ratio for high Fe content samples was 7.5 ± 5.8 with a major axis of 1468 μm , which are shown in Table 4.2 with the rest of the grain morphology measurements. Grain morphology in the HIP condition did not grow as much as expected and possible precipitate formation prevented significant grain growth.

Precipitates and secondary phases are known to form after post processing heat treatments of Inconel® 625 [8,36,54–56]. As shown in the EDS maps in Figure 5.7, low Fe content samples exhibited evidence of a high degree of segregation, which resulted in Mo and Nb rich precipitate formation with an average diameter of $0.84 \pm 0.22 \mu\text{m}$. In the high Fe content images, Mo or Nb precipitate formation is not observed. Expected elements that tend to have strong propensity to segregate instead dissociated into the matrix. Instead, small Ti rich precipitates with an average diameter of $0.5 \pm 0.2 \mu\text{m}$ are present.



(a)



(b)

Figure 5.6: EBSD images in the HIP condition of (a) low Fe and (b) high Fe

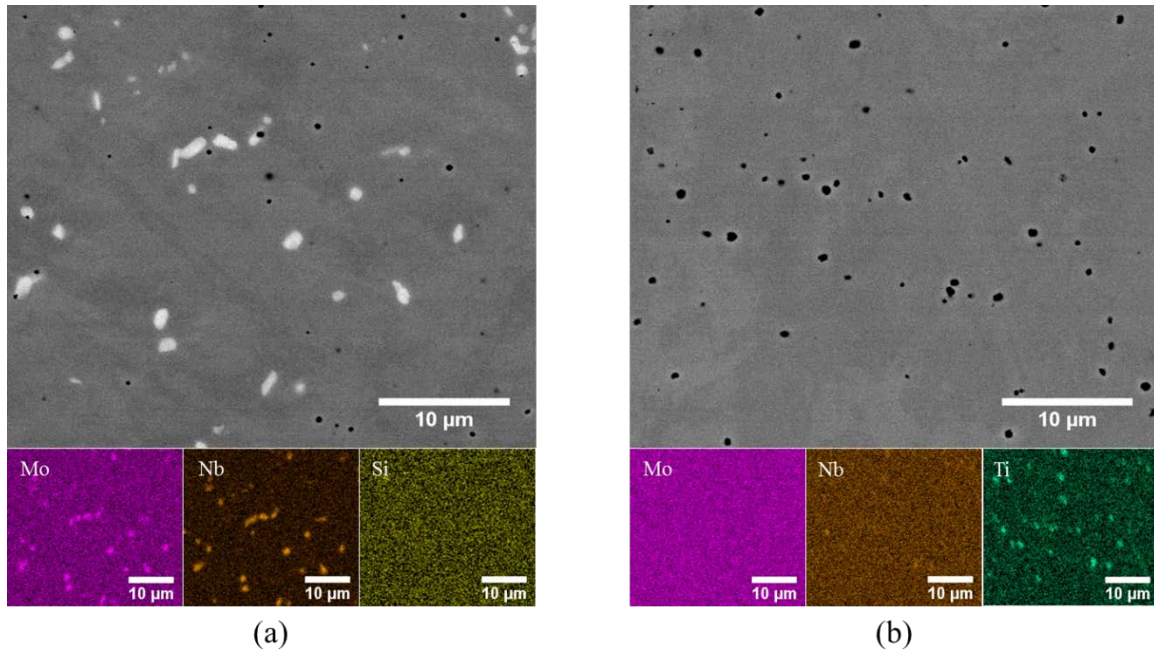


Figure 5.7: EDS maps of (a) low Fe and (b) high Fe in the HIP condition detailing the precipitation formation and the dissociation response in low Fe and high Fe.

Post-process heat treatments are typically characteristic of recrystallization and grain growth. However, between the as deposited and HIP condition samples, comparable grain morphologies are measured. It is speculated that the large Mo and Nb rich precipitates in the low Fe content samples are preventing grain growth at high temperatures. The size of precipitates is dictating which microstructural features are being pinned with larger precipitates impeding larger obstacles [57]. The large Mo and Nb precipitates are impeding the motion of grain boundaries in the low Fe content samples, which restricts grain growth. In the high Fe content samples, smaller Ti rich precipitates form that do not impede grain boundary motion but instead pin dislocations. This phenomenon resulted in the larger strain hardening exponent values. Figure 5.8 describes the two different phenomena that led to different strengthening mechanisms associated with the Fe content samples. Looking back at powder feedstock compositions, Fe additions were also combined with Ti additions from 0.019 wt % to 0.19 wt%, which is an order of magnitude increase. With sufficient levels of Nb, Ti additions have been known to be used for matrix refining purposes [8].

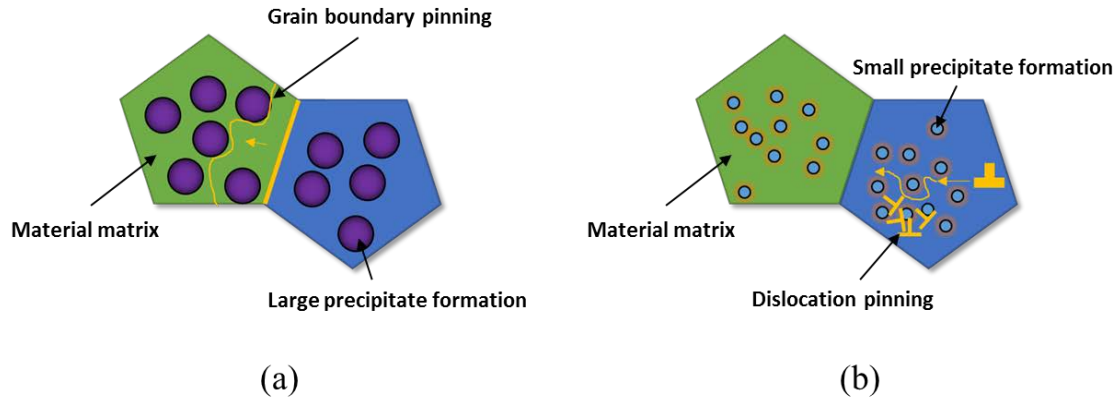


Figure 5.8: Diagrams describing the possible phenomena occurring in each HIP sample with respect to Fe content. In (a) the low Fe content case, large precipitates are impeding grain boundary motion and in (b) the high Fe content case, small precipitates, distributed readily are impeding dislocation motion.

5.2 Summary and Conclusions

Structures fabricated and characterized in the as deposited condition were further characterized in the post processing HIP condition. Identical characterization techniques were used to study the builds and comparisons were made between low and high Fe content HIP samples as well as to results in the as deposited condition. From the post processing study the following conclusion can be made:

- X-ray CT inspection confirmed that after the HIP treatment, no levels of defects were identified or seen in the inspection analysis. Defects that were present in the as deposited structures were not made out in the HIP structures while the same analysis parameters were used.
- Microstructural characterization showed that solidification structures disappeared and secondary phase formation was identified. Secondary phases were distributed through the material matrix and no significant changes in particle size or volume fraction were observed in the HIP samples. Similarities in the microstructure lead to comparable Vickers microhardness measurements in both Fe contents, however there was a sharp decreased in values compared to the as deposited measurements.
- Mechanical testing revealed differences between Fe contents for material strength and ductility. Low Fe content HIP specimens exhibited higher strengths but lower ductility. Similar to the as deposited condition, there was no dependence on tensile specimen

height or orientation. Compared to the as deposited mechanical properties, UTS values did not change as much as seen in the yield strength and elongation values. HIP specimens were found to increase the strain hardening induced during testing. As a result, low and high Fe content HIP UTS values resulted in values close to the as deposited UTS values. HIP specimens exhibited an increase in strain hardening and overall high Fe content specimens had higher strain hardening exponents.

- From the as deposited to HIP condition low Fe content samples still showed significantly smaller grains, on the order of 15x, compared to the average grain size of the high Fe content samples. In addition, EDS maps revealed Nb and Mo rich precipitate formation in Low Fe content samples however these two elements were dissociated into the matrix for high Fe content samples. Instead, Ti rich precipitates formed and were distributed through the matrix.
- Based on the mechanical properties, EBSD scans, and EDS maps the large Nb and Mo precipitates in the low Fe content are pinning grain boundaries, which result in small grains after HIP. Small Ti precipitates form in high Fe content samples, which are pinning dislocation motion.

Chapter 6

THEORIETICAL ANALYSIS OF PHASE STABILITY

In order to help explain the resulting secondary phase formation and characterize the type of constituents that formed, further investigation was done to understand the impact of Fe content. Presented in this chapter are thermodynamic calculations that help predict possible secondary phase formation and EPMA chemistry analyses that substantiate, which secondary phase are present.

6.1 Thermodynamic and Microstructural Characterization of the As Deposited Condition

6.1.1 Thermodynamic Stability

Preliminary thermodynamic calculations demonstrated that Fe content impacted the solidification of Inconel® 625. The solidification range is defined by the liquidus and solidus boundaries. Within this range, secondary phase constituents nucleate and grow until the melt pool temperature is below the solidus temperature. Initial calculations of the phase composition indicated that high Fe content Inconel® 625 had a solidification range of 263 K compared to a solidification range of 248 K for low Fe Inconel® 625. Expanding the solidification range increases the possible amount of secondary phase constituents that can form, as a result the crack susceptibility is increased [14]. During solidification, Mo and Nb partition to the liquid phase, which is seen in the as deposited condition where the interdendritic regions are rich in Mo and Nb as shown in Figure 6.1. The columnar dendrites are characteristic of high cooling rates. The dendrites arms that formed were rich in Ni, Cr, and Fe and seen in Figure 6.2 and Figure 6.3. How elements segregate is dependent on the distribution coefficient. Mo and Nb have distribution coefficients less than unity, which means these elements have strong segregation tendencies and segregate to the liquid during solidification. Cr, Fe, and Si have distribution coefficients near unit and therefore enrich the dendrite cores.

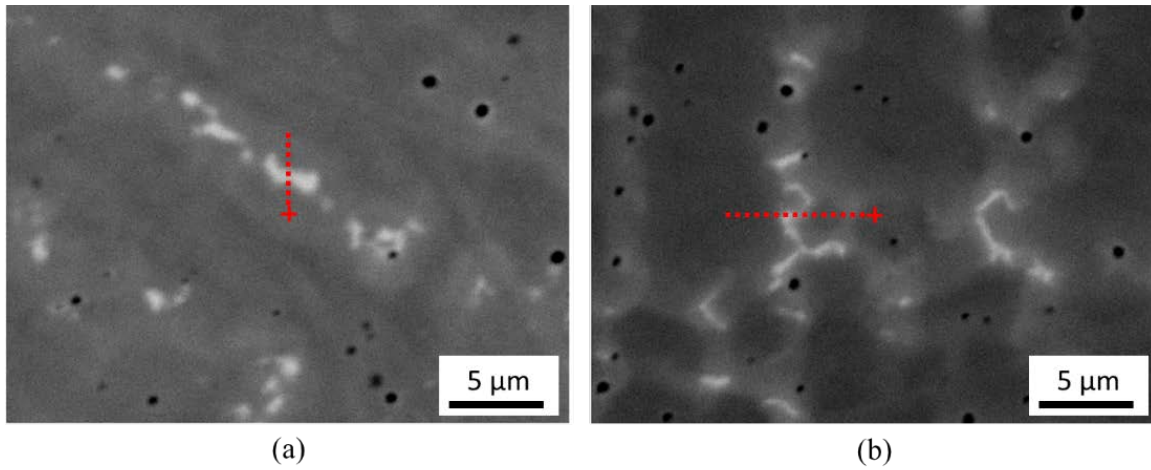


Figure 6.1: BSE photomicrographs of (a) low and (b) high Fe content microstructures denoting the EPMA line scan across interdendritic regions

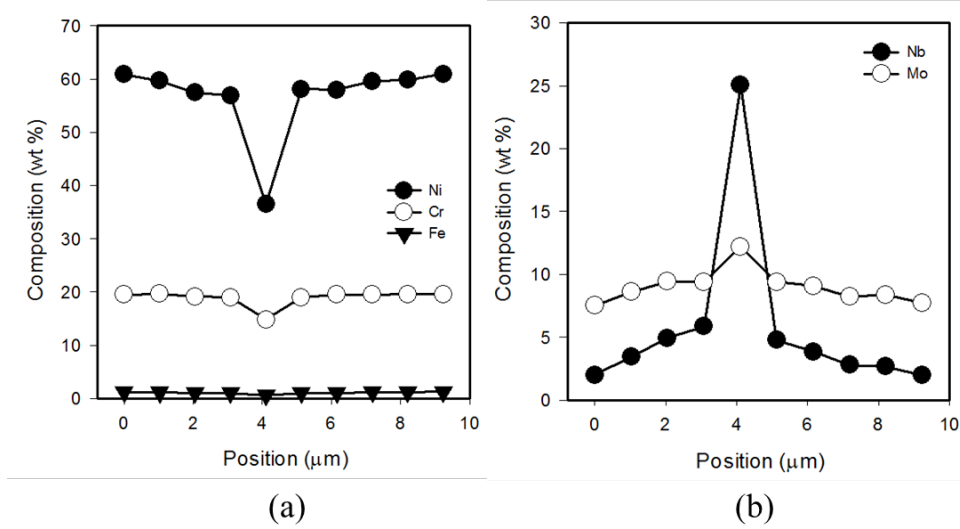


Figure 6.2: EMPA composition trace conducted across a low Fe content sample dendrite arm.

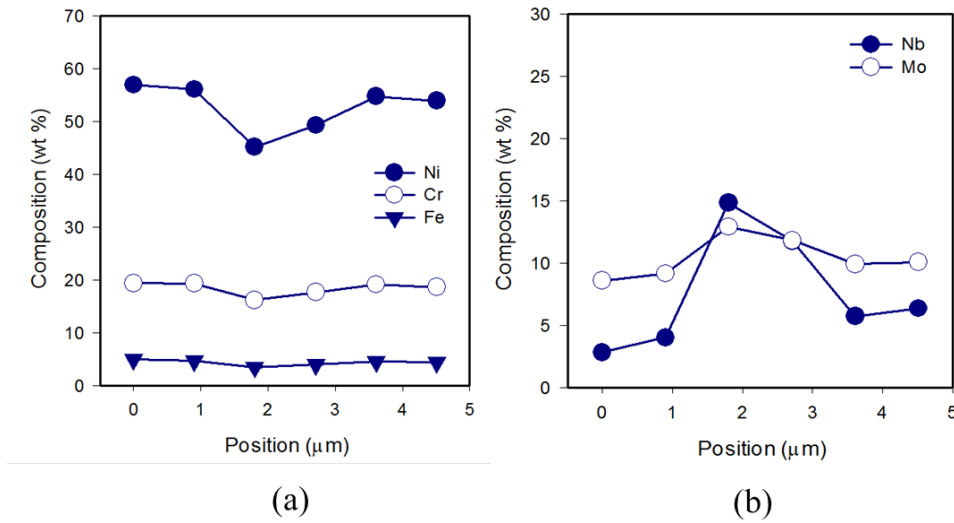
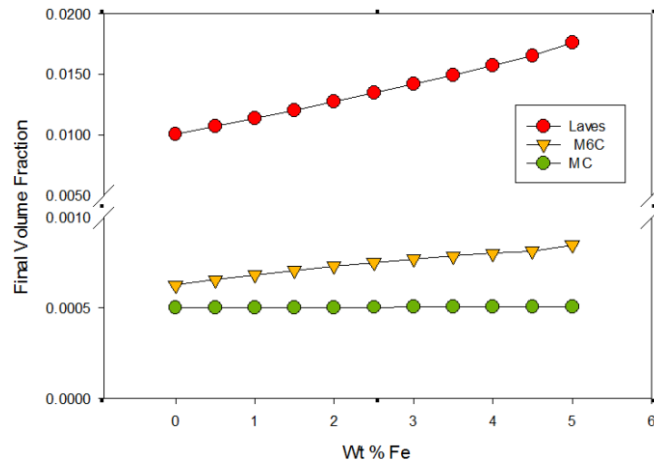


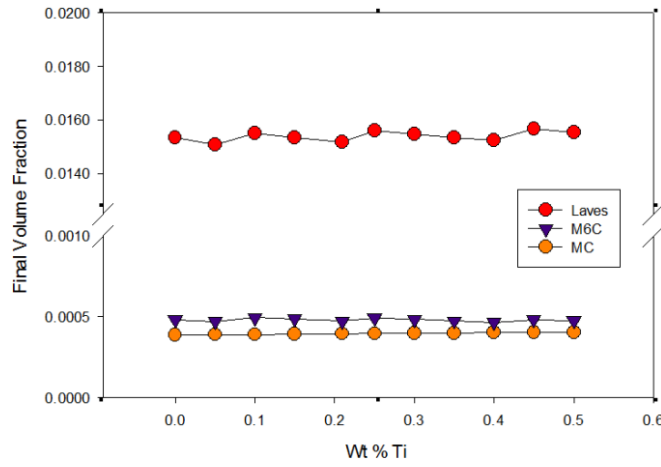
Figure 6.3: EMPA composition trace conducted across a high Fe content sample dendrite arm.

A compositional increase in the wt% Fe was also coupled with the addition of Ti and decrease in Si. Therefore, calculations were made to determine if secondary phase formation was influenced by the change in composition of Fe, Ti, and Si. Plots displaying secondary phase formation as a function of composition are shown in Figure 6.4. Specifically the formation of Laves phase, MC carbides, and M_6C carbides were looked at because previous work indicated secondary phase was primarily composed of one of these constituents [5,14]. Solidification routes of $L \rightarrow \gamma + \text{Laves}$ or $L \rightarrow \gamma + \text{NbC}$ are the most popular types of routes taken for Inconel® 625, however, Cieslak demonstrated that remaining Nb concentration could lead to a γ/M_6C constituent respectively, therefore it was also included in the plot.

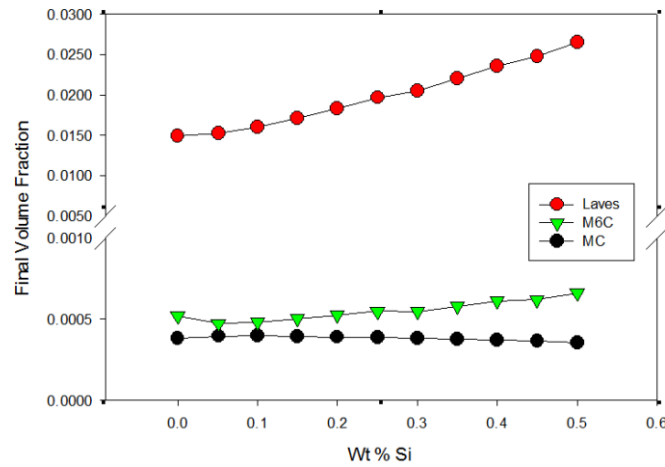
In order to differentiate between the possible secondary phase constituents, equilibrium phase calculations shown in Figure 6.5 display the Mo and Nb elemental compositions within each constituent. In order to be characterized as a Laves phase constituent, the Nb wt% would need to be approximately 30 wt%, 88 wt% for an NbC, and 28 wt% with Mo composition near 40 wt% for a M_6C . These plots also show during solidification, which constituent will form first. Initially, the liquid phase will partition into an NbC carbide, followed by a Laves phase constituent, and if enough Nb remains, a M_6C carbide will form. The solubility of Nb has been shown to be influenced by the addition of Fe content [3,14,20,21]. Though previous work indicated that the increase in Fe inhibited Nb solubility, at equilibrium shown in Figure 6.6, there is a small change in the composition of Nb in the matrix.



(a)



(b)



(c)

Figure 6.4: Thermodynamic calculations that show the influence of various alloying elements (a) Fe; (b) Ti; (c) Si on secondary phase formation.

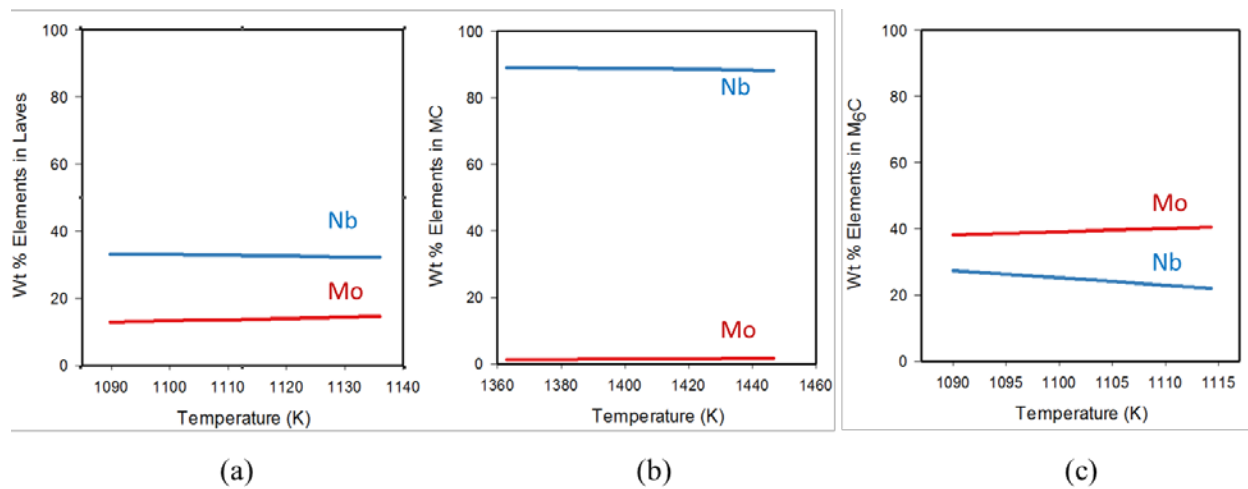


Figure 6.5: Representative wt% compositions of Nb and Mo in specific secondary phases: (a) Laves phase; (b) MC carbide; (c) M_6C carbide. Nb wt% can be used to identify which secondary phase is forming after solidification.

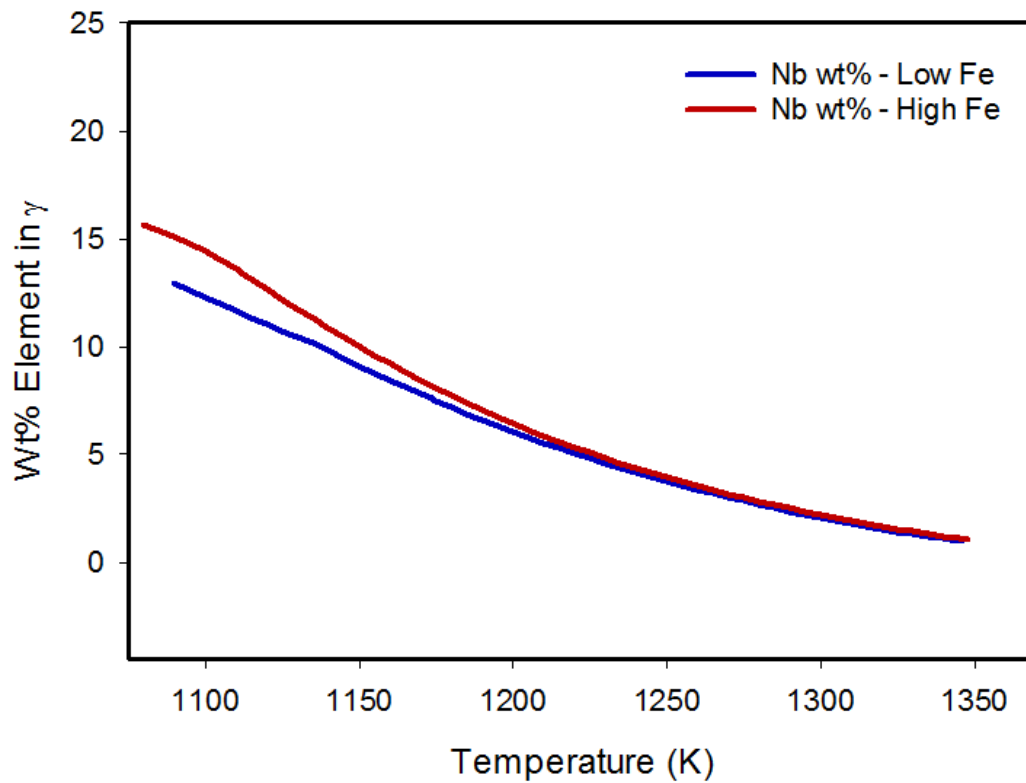


Figure 6.6: Element composition of Nb wt% in matrix (γ) as a function of temperature. The Nb wt% compositional is higher in the high Fe content Inconel® 625.

6.1.2 Characterization of the Secondary Phase

EPMA analysis helped characterize the resulting secondary phase formation in the as deposited condition. Point specific quantitative compositional measurements were made to identify secondary phase formation, which are shown and listed in Figure 6.7 and Table 6.1. The morphological shape of the constituent would appear to be Laves phase based on previous secondary phase characterization work [5,13]. The measured composition of Nb, which is listed in Table 6.1, for the secondary phase constituent is between 17 – 25wt%. As a result, this supports the equilibrium phase calculations in Figure 6.5 because the Nb and Mo compositions are too low to be considered an NbC or M₆C carbide.

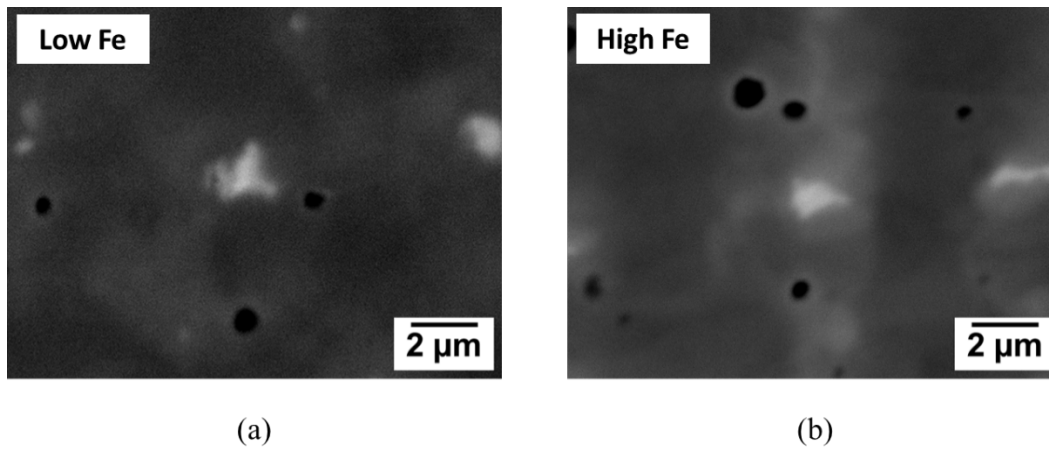


Figure 6.7: EPMA chemistry analysis of the resulting secondary phase constituents that formed in the as deposited condition for (a) low Fe and (b) high Fe content samples.

Table 6.1: Chemical compositions of the constituents shown in Figure 6.7.

Element	Wt % of Secondary Phase Constituent	
	Low Fe	High Fe
Ni	35.95	41.25
Cr	17.02	15.55
Nb	24.21	17.82
Mo	12.21	15.19
Fe	0.63	3.33

In addition, another way to characterize the secondary phase formation is using the C/Nb ratio [20]. When the C content is minimal so that the C/Nb ratio is low, Laves phase is the dominating constituent. Based on literature that would characterize and identify the resulting constituents produced after welding operations, carbides would only form with sufficient amount of C in the initial feedstock material [5,13,20,21]. Therefore, when C content is increased, the formation of carbides, along with Laves phase, would then be expected to form. From the chemical composition for both low and high Fe content powder feedstock samples, Laves phase would be expected. The C content is 0.008 wt%, which is very low and therefore very little C can be utilized to promote carbide formation. In combination with the EPMA measurements, the primary secondary phase constituents that are forming in the low and high Fe content samples in the as deposited condition are presumably Laves phase.

6.2 Thermodynamic and Microstructural Characterization of the HIP Condition

6.2.1 Thermodynamic Stability

In the HIP condition, Mo and Nb rich precipitates are observed in the low Fe content samples, but Ti rich precipitates formed in the high Fe content samples. Changes in chemistries lead to possible speculation that the increase in Ti composition promoted MC carbide formation. In order to study the solute segregation during solidification of the HIP samples, Scheil solidification calculations were conducted. The phase stability of low and high Fe content samples during solidification is shown in Figure 6.8. Overall, negligible amounts of secondary phase are expected to form. However, as shown in Figure 6.8b, MC phase formation is stable at the HIP temperature (1533 K) while no MC phase is present for the low Fe content samples. The differences in phase stability for low and high Fe HIP samples impact the microstructure which was initially seen in Figure 5.7 of the EDS maps in chapter 5.

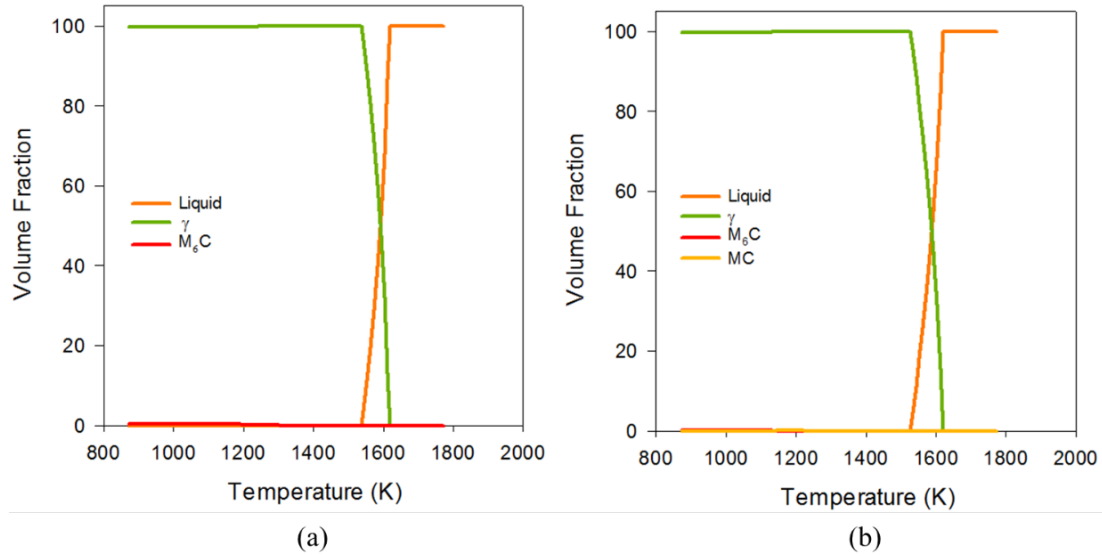


Figure 6.8: Scheil calculations of the resulting phase fraction upon solidification for (a) low Fe and (b) high Fe content compositions. The HIP treatment was conducted at 1433 K. MC carbide formation is present in the high Fe content calculation but not for low Fe.

6.2.2 Microstructural Characterization of Secondary Phase Constituents

Quantifying the elemental compositions of each secondary phase constituent for low and high Fe samples was done using EPMA. Because no identifiable Laves or carbide phase formed in the high Fe content HIP samples, another analysis was conducted on the dark spots that were distributed throughout the matrix. The measured compositions are listed in Table 6.2 and the point analysis areas that were analyzed are shown in Figure 6.9. In the low Fe content HIP sample, the composition of Mo and Nb wt% is indicative of Laves phase. Compositional matrix values were measured in the high Fe content sample, respectively. An additional chemical analysis was conducted on the high Fe content HIP sample as shown in Figure 6.10 and found that the dark sports were enriched with approximately 10 wt% Ti. There was minor intensity pick up of Nb near these Ti precipitates, which would support the argument that for matrix refining purposes, Ti would need to be combined with Nb [8].

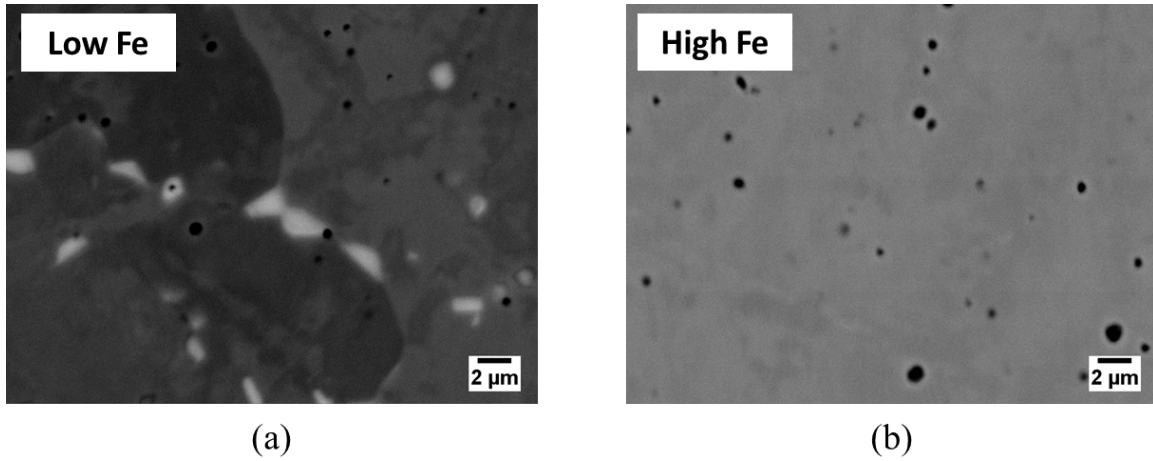


Figure 6.9: EPMA chemistry analysis of the resulting secondary phase constituents that formed in the HIP condition for (a) low Fe and (b) high Fe content samples.

Table 6.2: Chemical compositions of the constituents that formed in the HIP condition.*High Fe content samples do not form Laves phase or carbides.

Element	Wt % of Secondary Phase Constituent		Ti rich Precipitates
	Low Fe	High Fe*	High Fe
Ni	32.54	56.54	36.25
Cr	13.90	18.88	15.41
Nb	22.59	3.54	17.05
Mo	18.90	8.54	5.49
Fe	0.45	4.89	2.57
Ti	—	—	9.94

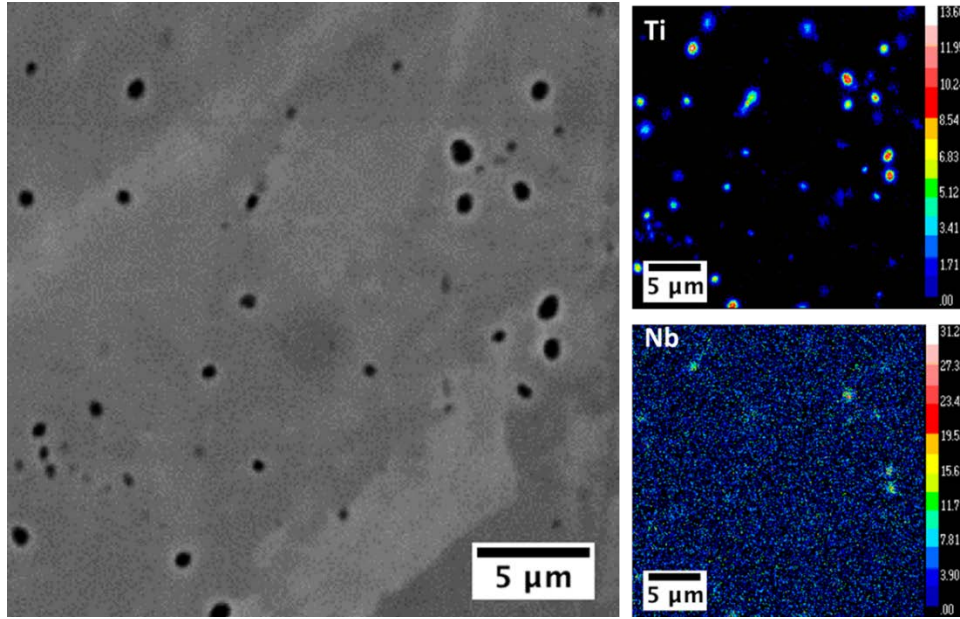


Figure 6.10: EPMA chemistry map analysis portraying measureable Ti intensity specifically where black spots are located in the BSE image. The color scale is in wt%.

6.3 Summary and Conclusions

The impact of chemistry on resulting secondary phase formation was identified using characterized using EPMA and phase stability calculations. At the HIP temperature, the various combinations of alloying elements can impact what secondary phase constituent forms. Findings from this chapter include:

- The resulting secondary phase constituents are Laves phase due to the measured Nb wt.% from EPMA and the low C content in the powder feedstock material.
- Based upon the phase stability calculations for the two different powder feedstock compositions. At the HIP temperature, MC carbide formation was stable for high Fe content Inconel® 625 and M_6C carbide formation was stable for low Fe content Inconel® 625.

Chapter 7

CONCLUDING REMARKS

7.1 Summary and Conclusions

Additive manufacturing is an enabling technology that has capitalized on the technological innovation that has occurred over the previous decades. Laser processing improved, robotics advanced, and equipment costs have decreased. However, there is one factor that has not been improved upon and that is the powder feedstock material. Results in this thesis have demonstrated the need to control powder composition should be considered for AM work. Cieslak et al. initially brought alloying element composition to the forefront with the factorially-designed Inconel® 625 alloy element matrix [5,13]. Floreen et al. concluded that in order to produce consistent, reliable components tighter controls of the alloying composition needed to be made [8]. Numerous factors have been improved that has led to the mainstream publicity of AM. However, the powder characterization techniques used for the welding operations in the past are still being implemented to validate powder feedstock material in the same way but now the feedstock material is utilized for AM processes.

Analysis of the Inconel® 625 system for Fe contents at the 1 wt% and 4 wt% were investigated. The Fe content addition was also coupled with a compositional increase in Ti and a decrease in Si. Characterization the AM DED fabricated structure showed no differences after preliminary metallurgical characterization of the microstructure was conducted. It was not until mechanical testing was preformed that changes in the resulting properties for the two powder feedstock materials was identified. Low Fe content samples exhibited higher strengths and lower ductility. For both samples in the as deposited condition, alloying elements segregated similarly with Nb and Mo partitioning into the interdendritic regions and Ni, Cr, and Fe enriching the dendrite arms. The primary strengthening mechanism in the as deposited condition was grain size. The average grain size area in the high Fe content samples was ten times larger than the average grain size in the low Fe content samples. Therefore, strength was minimized for higher Fe contents and improvement in the ductility was reported.

A standard HIP treatment was conducted on the as deposited DED structures to remove the possible defect formation via lack of fusion or porosity. Microstructurally, materials responded similarly to each other with no defect formation detected, the solidification structures disappeared

leaving only secondary phase constituents, and the hardness significantly decreased compare to the as deposited condition. Low Fe content HIP samples reported higher strengths and lower ductility. However compared to the as deposited condition mechanical results, there was little change in the reported UTS HIP value. In response to being exposed to the HIP temperature and held there for elongated times, HIP tensile specimens exhibited higher strain hardening exponents, which diminished the large difference in yield strength and led to the as deposited and HIP UTS values for each Fe content samples to be comparable. Grain size differences remained consistent between low and high Fe content samples. Possible explanation of the varying mechanical property results is due to the secondary phase formation after HIP. Low Fe content samples formed large blocky, irregularly shaped Mo and Nb rich precipitates which are assumed to be Laves phase while in the high Fe content samples, Mo and Nb dissociated into the matrix. Instead, smaller spherical Ti rich precipitates formed in the high Fe content samples. Precipitates in the low Fe content samples are pinning grain boundary motion which restricts grain growth for the HIP samples and therefore increases the strength. Ti precipitates impede dislocation motion, which increases the strain hardening exponents in the high Fe samples. Thermodynamic calculations confirmed the phase stability of an MC carbide near the HIP temperature. EPMA chemical mapping revealed that the dark spot formation seen in BSE imaging corresponded with Ti rich intensities signifying Ti rich precipitates.

7.2 Future Work

In order to determine the exact role Fe content has on the Inconel® 625 system, additional research directions should be explored. More alloy compositions should be investigated and the Si and Ti compositions should be carefully examined. Low Fe, low Si, and low Ti content Inconel® 625 should be compared with high Fe, Si, and Ti content in order to set fundamental boundaries of the Ni base system. In addition, secondary phase could be characterize more in depth using DTA and TEM. DTA would supplement the computational results in this study with experimental results on whether the alloying additions would increase or decrease the liquid and solidus temperatures and solidification temperature range. TEM would provide a high quality in depth characterization of the morphology and chemical composition of the resulting secondary phase constituents in both the as deposited and HIP conditions. A TEM chemical analysis would be able to discriminate between Laves phase or carbide formation, which would allow powder composition to be adjusted in order to intentionally mitigate or exacerbate secondary phase

formation. The expansion of knowledge for common AM deposited materials is growing, however attention must be directed to powder composition in order to continually innovate the manufacturing field.

REFERENCES

- [1] C. Thomas, P. Tait, The performance of Alloy 625 in long-term intermediate temperature applications, *Int. J. Press. Vessel. Pip.* 59 (1994) 41–49. doi:10.1016/0308-0161(94)90140-6.
- [2] Inconel Alloy 625, Spec. Met. Corp. (2013).
- [3] J.N. DuPont, J.C. Lippold, S.D. Kiser, *Welding Metallurgy and Weldability of Nickel-Base Alloys*, John Wiley & Sons, Inc., Hoboken, New Jersey, 2009.
- [4] D.J.T. and S.J.P. G. D. Smith, Alloy 625 - Impressive Past/Significant Presence/Awesome Future, *Superalloys 718, 625, 706 Var. Deriv.* (2001) 35–46. doi:10.7449/2001/Superalloys_2001_35_46.
- [5] M.J. Cieslak, The welding and solidification metallurgy of Alloy 625, *Weld. J.* 70 (1991) 49–56.
- [6] L.E. Murr, E. Martinez, S.M. Gaytan, D.A. Ramirez, B.I. MacHado, P.W. Shindo, J.L. Martinez, F. Medina, J. Wooten, D. Ciscel, U. Ackelid, R.B. Wicker, Microstructural architecture, microstructures, and mechanical properties for a nickel-base superalloy fabricated by electron beam melting, *Metall. Mater. Trans. A Phys. Metall. Mater. Sci.* 42 (2011) 3491–3508. doi:10.1007/s11661-011-0748-2.
- [7] M.J. Cieslak, G.A. Knorovsky, T.J. Headley, A.D. Romig, The use of new PHACOMP in understanding the solidification microstructure of nickel base alloy weld metal, *Metall. Trans. A.* 17 (1986) 2107–2116. doi:10.1007/BF02645909.
- [8] S. Floreen, G.E. Fuchs, W.J. Yang, The Metallurgy of Alloy 625, *Superalloys.* (1994) 13–37. doi:10.7449/1994/Superalloys_1994_13_37.
- [9] G.D. Janaki Ram, A. Venugopal Reddy, K. Prasad Rao, G. Madhusudhan Reddy, Control of Laves phase in Inconel 718 GTA welds with current pulsing, *Sci. Technol. Weld. Join.* 9 (2004) 390–398. doi:10.1179/136217104225021788.
- [10] P. Nie, O.A. Ojo, Z. Li, Numerical modeling of microstructure evolution during laser additive manufacturing of a nickel-based superalloy, *Acta Mater.* 77 (2014) 85–95. doi:10.1016/j.actamat.2014.05.039.
- [11] K.-M. Chang, H.-J. Lai, J.-Y. Hwang, Existence of Laves Phase in Nb-Hardened Superalloys, *Superalloys 718, 625, 706 Var. Deriv.* (1994) 683–694. doi:10.7449/1994/Superalloys_1994_683_694.

- [12] M. Rombouts, G. Maes, M. Mertens, W. Hendrix, Laser metal deposition of Inconel 625: Microstructure and mechanical properties, *J. Laser Appl.* 24 (2012) 52007. doi:10.2351/1.4757717.
- [13] M.J. Cieslak, T.J. Headley, A.D. Romig, T. Kollie, A melting and solidification study of alloy 625, *Metall. Trans. A.* 19 (1988) 2319–2331. doi:10.1007/BF02645056.
- [14] J.N. DuPont, Solidification of an alloy 625 weld overlay, *Metall. Mater. Trans. A.* 27 (1996) 3612–3620. doi:10.1007/BF02595452.
- [15] J.C. Heigel, P. Michaleris, T.A. Palmer, In situ monitoring and characterization of distortion during laser cladding of Inconel® 625, *J. Mater. Process. Technol.* 220 (2015) 135–145. doi:10.1016/j.jmatprotec.2014.12.029.
- [16] J.C. Heigel, P. Michaleris, T.A. Palmer, Measurement of forced surface convection in directed energy deposition additive manufacturing, *Proc. Inst. Mech. Eng. Part B J. Eng. Manuf.* 230 (2016) 1295–1308. doi:10.1177/0954405415599928.
- [17] J.C. Heigel, M.F. Gouge, P. Michaleris, T.A. Palmer, Selection of powder or wire feedstock material for the laser cladding of Inconel 625, *J. Mater. Process. Technol.* 231 (2016) 357–365. doi:10.1016/j.jmatprotec.2016.01.004.
- [18] C.C. Silva, H.C. De Miranda, M.F. Motta, J.P. Farias, C.R.M. Afonso, A.J. Ramirez, New insight on the solidification path of an alloy 625 weld overlay, *J. Mater. Res. Technol.* 2 (2013) 228–237. doi:10.1016/j.jmrt.2013.02.008.
- [19] W.E. Frazier, Metal additive manufacturing: A review, *J. Mater. Eng. Perform.* (2014). doi:10.1007/s11665-014-0958-z.
- [20] J.N. DuPont, C. V Robino, J.R. Michael, M.R. Notis, A.R. Marder, Solidification of Nb-bearing superalloys: Part I. Reaction sequences, *Metall. Mater. Trans. a-Physical Metall. Mater. Sci.* 29 (1998) 2785–2796. doi:10.1007/s11661-998-0319-3.
- [21] J.N. DuPont, A.R. Marder, M.R. Notis, C. V. Robino, Solidification of Nb-bearing superalloys: Part II. Pseudoternary solidification surfaces, *Metall. Mater. Trans. A.* 29 (1998) 2797–2806. doi:10.1007/s11661-998-0320-x.
- [22] Y. Kakinuma, M. Mori, Y. Oda, T. Mori, M. Kashiwara, A. Hansel, M. Fujishima, Influence of metal powder characteristics on product quality with directed energy deposition of Inconel 625, *CIRP Ann. - Manuf. Technol.* 65 (2016) 209–212. doi:10.1016/j.cirp.2016.04.058.

- [23] T.E. Abioye, J. Folkes, A.T. Clare, A parametric study of Inconel 625 wire laser deposition, *J. Mater. Process. Technol.* 213 (2013) 2145–2151. doi:10.1016/j.jmatprotec.2013.06.007.
- [24] E.R. Denlinger, J.C. Heigel, P. Michaleris, T.A. Palmer, Effect of inter-layer dwell time on distortion and residual stress in additive manufacturing of titanium and nickel alloys, *J. Mater. Process. Tech.* 215 (2015) 123–131. doi:10.1016/j.jmatprotec.2014.07.030.
- [25] C.P. Paul, P. Ganesh, S.K. Mishra, P. Bhargava, J. Negi, A.K. Nath, Investigating laser rapid manufacturing for Inconel-625 components, *Opt. Laser Technol.* (2007). doi:10.1016/j.optlastec.2006.01.008.
- [26] K. Amato, Comparison of Microstructures and Properties for a Ni-Base Superalloy (Alloy 625) Fabricated by Electron Beam Melting, *J. Mater. Sci. Res.* 1 (2012) p3. doi:10.5539/jmsr.v1n2p3.
- [27] G.P. Dinda, A.K. Dasgupta, J. Mazumder, Laser aided direct metal deposition of Inconel 625 superalloy: Microstructural evolution and thermal stability, *Mater. Sci. Eng. A.* (2009). doi:10.1016/j.msea.2009.01.009.
- [28] Z. Wang, E. Denlinger, P. Michaleris, A.D. Stoica, D. Ma, A.M. Beese, Residual stress mapping in Inconel 625 fabricated through additive manufacturing: Method for neutron diffraction measurements to validate thermomechanical model predictions, *Mater. Des.* 113 (2017). doi:10.1016/j.matdes.2016.10.003.
- [29] P. Ganesh, R. Kaul, C.P. Paul, P. Tiwari, S.K. Rai, R.C. Prasad, L.M. Kukreja, Fatigue and fracture toughness characteristics of laser rapid manufactured Inconel® 625 Structures, *Mater. Sci. Eng. A.* (2010). doi:10.1016/j.msea.2010.08.034.
- [30] N.H. Sateesh, G.C.M. Kumar, K. Prasad, S. C.K., A.R. Vinod, Microstructure and Mechanical Characterization of Laser Sintered Inconel-625 Superalloy, *Procedia Mater. Sci.* 5 (2014) 772–779. doi:10.1016/j.mspro.2014.07.327.
- [31] A. Kreitchberg, V. Brailovski, S. Turenne, Effect of heat treatment and hot isostatic pressing on the microstructure and mechanical properties of Inconel 625 alloy processed by laser powder bed fusion, *Mater. Sci. Eng. A.* 689 (2017) 1–10. doi:10.1016/j.msea.2017.02.038.
- [32] T. Mukherjee, J.S. Zuback, A. De, T. DebRoy, Printability of alloys for additive manufacturing., *Sci. Rep.* 6 (2016) 19717. doi:10.1038/srep19717.

- [33] W.J. Sames, F.A. List, S. Pannala, R.R. Dehoff, S.S. Babu, The metallurgy and processing science of metal additive manufacturing, *Int. Mater. Rev.* 61 (2016) 315–360. doi:10.1080/09506608.2015.1116649.
- [34] B.K. Foster, A.M. Beese, J.S. Keist, E.T. McHale, T.A. Palmer, Impact of Interlayer Dwell Time on Microstructure and Mechanical Properties of Nickel and Titanium Alloys, *Metall. Mater. Trans. A.* 48 (2017) 1–12. doi:10.1007/s11661-017-4164-0.
- [35] E.A. Lass, M.R. Stoudt, M.E. Williams, M.B. Katz, L.E. Levine, T.Q. Phan, T.H. Gnaeupel-Herold, D.S. Ng, Formation of the Ni₃Nb δ -Phase in Stress-Relieved Inconel 625 Produced via Laser Powder-Bed Fusion Additive Manufacturing, *Metall. Mater. Trans. A Phys. Metall. Mater. Sci.* 48 (2017) 1–12. doi:10.1007/s11661-017-4304-6.
- [36] T. Keller, G. Lindwall, S. Ghosh, L. Ma, B.M. Lane, F. Zhang, U.R. Kattner, E.A. Lass, J.C. Heigel, Y. Idell, M.E. Williams, A.J. Allen, J.E. Guyer, L.E. Levine, Application of finite element, phase-field, and CALPHAD-based methods to additive manufacturing of Ni-based superalloys, *Acta Mater.* (2017). doi:10.1016/j.actamat.2017.05.003.
- [37] F. Zhang, L.E. Levine, A.J. Allen, C.E. Campbell, E.A. Lass, S. Cheruvathur, M.R. Stoudt, M.E. Williams, Y. Idell, Homogenization kinetics of a nickel-based superalloy produced by powder bed fusion laser sintering, *Scr. Mater.* 131 (2017) 98–102. doi:10.1016/j.scriptamat.2016.12.037.
- [38] A. B213, Standard Test Methods for Flow Rate of Metal Powders Using the Hall Flowmeter Funnel, *i* (2014) 213–216. doi:10.1520/B0213-13.2.
- [39] H.F. Funnel, Standard Test Method for Apparent Density of Free-Flowing Metal Powders Using the Hall Flowmeter Funnel, *ASTM Int.* 2 (1999) 89–91. doi:10.1520/B0212-13.2.
- [40] International ASTM, Standard Test Method for Tap Density of Metal Powders and Compounds, *ASTM Int.* (2015) 15–18. doi:10.1520/B0527-15.2.
- [41] A. C1444, Standard Test Method for Measuring the Angle of Repose of Free-Flowing Mold Powders, *ASTM Int.* (2000) 15–16. doi:10.1520/C1444-00.
- [42] ASTM B705 – 05, Standard Specification for Nickel-Alloy (UNS N06625 , N06219 and N08825) Welded Pipe, *ASTM Int.* 5 (2015) 3–5. doi:10.1520/B0705-05R09.
- [43] R. Tandon, T. Wilks, M. Gieseke, C. Noelke, S. Kaierle, T. Palmer, Additive Manufacturing of Elektron® 43 Alloy Using Laser Powder Bed and Directed Energy Deposition, *Euro PM2015.* (2015).

- [44] J.S. Keist, T.A. Palmer, Role of geometry on properties of additively manufactured Ti-6Al-4V structures fabricated using laser based directed energy deposition, *Mater. Des.* 106 (2016) 482–494. doi:10.1016/j.matdes.2016.05.045.
- [45] J.J. Blecher, T.A. Palmer, T. Debroy, Solidification Map of a Nickel-Base Alloy, (n.d.). doi:10.1007/s11661-013-2149-1.
- [46] ASTM E8/E8M-15a, Standard Test Methods for Tension Testing of Metallic Materials 1, ASTM Int. (2009) 1–27. doi:10.1520/E0008.
- [47] ASTM E646, Standard Test Method for Tensile Strain-Hardening Exponents (n-Values) of Metallic Sheet Materials, ASTM Int. 3 (2000) 1–8. doi:10.1520/E0646-07E01.2.
- [48] R. German, Powder Metallurgy and Particulate Material Processing, in: Metal Powder Industries Federation, Princeton, New Jersey, 2005: pp. 45-46-129.
- [49] O.D. Neikov, D. V. Lotsko, V.G. Gopienko, Powder characterization and testing, Elsevier Ltd, 2009. doi:10.1016/B978-1-85617-422-0.00001-X.
- [50] Z. Wang, T.A. Palmer, A.M. Beese, Effect of processing parameters on microstructure and tensile properties of austenitic stainless steel 304L made by directed energy deposition additive manufacturing, *Acta Mater.* 110 (2016) 226–235. doi:10.1016/j.actamat.2016.03.019.
- [51] J.S. Keist, T.A. Palmer, Development of strength-hardness relationships in additively manufactured titanium alloys, *Mater. Sci. Eng. A.* 693 (2017) 214–224. doi:http://dx.doi.org/10.1016/j.msea.2017.03.102.
- [52] J.J. Lewandowski, M. Seifi, Metal Additive Manufacturing: A Review of Mechanical Properties, *Annu. Rev. Mater. Res.* 46 (2016) 151–186. doi:10.1146/annurev-matsci-070115-032024.
- [53] Q. Guo, D. Li, S. Guo, H. Peng, J. Hu, The effect of deformation temperature on the microstructure evolution of Inconel 625 superalloy, *J. Nucl. Mater.* 414 (2011) 440–450. doi:10.1016/j.jnucmat.2011.05.029.
- [54] M. Sundararaman, P. Mukhopadhyay, S. Banerjee, Carbide precipitation in nickel base superalloys 718 and 625 and their effect on mechanical properties, *TMS Superalloys 718*. (1997) 625–706. doi:10.7449/1997/Superalloys_1997_367_378.
- [55] C. Cortial, F., Corrieu, J. M., and Vernot-Loier, Influence of heat treatment on microstructure, Mechanical Properties and Corrosion Resistance of weld alloy 625.pdf,

- Metall. Mater. Trans. a. 26A (1995) 1273–1286. doi:10.1007/BF02670621.
- [56] V. Shankar, K. Bhanu Sankara Rao, S.L. Mannan, Microstructure and mechanical properties of Inconel 625 superalloy, J. Nucl. Mater. 288 (2001) 222–232. doi:10.1016/S0022-3115(00)00723-6.
- [57] Y. Liao, C. Ye, H. Gao, B. Kim, S. Suslov, Y. Liao, C. Ye, H. Gao, B. Kim, S. Suslov, E.A. Stach, Dislocation pinning effects induced by nano-precipitates during warm laser shock peening : Dislocation dynamic simulation and experiments Dislocation pinning effects induced by nano-precipitates during warm laser shock peening : Dislocation dynamic simula, 23518 (2011). doi:10.1063/1.3609072.